2015

Analysis of Polar Mesocyclonic Surface Turbulent Fluxes in the Arctic System Reanalysis (ASRv1) Dataset

Kyle Kevin Ahern

FLORIDA STATE UNIVERSITY

COLLEGE OF ARTS AND SCIENCES

ANALYSIS OF POLAR MESOCYCLONIC SURFACE TURBULENT FLUXES IN THE ARCTIC SYSTEM REANALYSIS (ASRV1) DATASET

By

KYLE KEVIN AHERN

A Thesis submitted to the
Department of Earth, Ocean, and Atmospheric Science
in partial fulfillment of the
requirements for the degree of
Master of Science

2015

Kyle K. Ahern defended this thesis on July 10, 2015.

The members of the supervisory committee were:

Mark A. Bourassa
Professor Directing Thesis

Robert E. Hart
Committee Member

Henry E. Fuelberg
Committee Member

The Graduate School has verified and approved the above-named committee members, and certifies that the thesis has been approved in accordance with university requirements.

For my father, who could only imagine.

ACKNOWLEDGEMENTS

I thank my major professor, Dr. Mark Bourassa, for reaching out and giving me the opportunity to pursue a graduate degree. I am grateful for his allowance of fulfilling scientific curiosities and networking capabilities, as well as his insistence on continuing to learn new things. I also thank my committee members, Dr. Robert Hart and Dr. Henry Fuelberg, for their continued support and honest advice. They have been instrumental through research and academics since my undergraduate studies, and their help is always both enlightening and humbling. Without the support of my three committee members, this work would have been impossible.

I thank my family, who have supported me from the very beginning in any way they can; particularly my mother, who has been a symbol of strength in the face of incredible adversity and hardship. I thank my friends, who keep me grounded and have kept me relatively sane through the arduous tasks and complications of graduate life.

TABLE OF CONTENTS

LIST OF FIGURES

ABSTRACT

Maritime mesocyclones form throughout the year at the polar latitudes, often near or embedded within cloud streets associated with massive cold air outbreaks. Such storms appear on the 50 – 1000 km horizontal scale. However, polar mesocyclones tend to exist on the smaller end of the horizontal scale. As a storm's size decreases, the likelihood that they will be well-represented in data also decreases. Underrepresentation of polar mesocyclones in reanalyses will affect climatological forecasts and research that utilize such data. Namely, the air-sea interactions associated with polar mesocyclones will be underrepresented, thereby impacting estimates of ocean circulation. Additionally, many reanalyses underestimate near-surface wind speeds, which is linked to but not exclusively dependent on the problems associated with data resolution. Harsh polar conditions make these regions of scientific interest unfavorable for in situ data collection, which compounds the aforementioned issues.

This research examines the relatively new Arctic System Reanalysis (ASRv1) and its ability to represent three polar mesocyclonic systems of differing size. Should ASRv1 represent polar mesocyclones effectively, it could be a prime candidate for establishing an arctic atmospheric state for air-sea modeling. The product is compared to high-resolution Weather Research and Forecasting (WRF) model simulations, with ERA-Interim information providing the initial and boundary conditions. Simulation results are checked against available 10 m equivalent neutral wind data from QuikSCAT to ensure that the model is producing reasonable atmospheric conditions. Comparisons are drawn for near-surface wind fields and surface turbulent fluxes to focus on ASRv1's depictions of the air-sea interactions associated with polar mesocyclones.

Differences between ASRv1 and the WRF simulations are presented with their likely explanations—physical, dynamical, and data-based (e.g., resolution, model options).

CHAPTER ONE

INTRODUCTION

Oceanic and atmospheric processes are driven by surface turbulent fluxes at the air-sea boundary, which allow the exchange of momentum and heat between the atmosphere and the ocean. Wind stress and heat fluxes contribute to driving oceanic convection, both near the surface and in the deep ocean. A continual loss of heat from the ocean at the air-sea boundary reduces near-surface water temperature, which increases its density and reduces vertical stratification in the local water column. Evaporation and freshwater flux at the air-sea boundary can also alter the near-surface water density though consequential changes in salinity. Near the winter poles, the sustained loss of heat from a warm ocean relative to the atmosphere is expected. A persistent erosion of vertical stratification can eventually allow areas of open-ocean convection to develop; the surface waters sustain such a reduction of buoyancy that they sink to intermediate or deeper depths (Marshall and Schott 1999).

As noted in Marshall and Schott (1999) and Condron et al. (2008), particular North Atlantic maritime regions such as the Greenland Sea are home to potentially deep open-ocean convection. Such convection in the Greenland Sea and the other Nordic Seas (Norwegian and Iceland Seas) effects the thermohaline circulation—the global meridional overturning circulation (GMOC) that connects equatorial and polar waters. The GMOC transports warm, salty equatorial water toward the poles, where it may sink to depth and return toward the subpolar North Atlantic. Previous work suggests that volumetric water transport from the Nordic Seas to the subarctic North Atlantic influences the strength of the GMOC through its impact on compensating northward water transport near the surface (Rahmstorf 1995; Rahmstorf 1996; Latif et al. 2006). Through the link

between vertical water transport in the Nordic Seas and the strength of the GMOC, it follows that the amount of vertical transport in that region should incite responses from the climate system (Bacon 1998; Clark et al. 2002; McManus et al. 2004; Pickart and Spall 2007).

As the atmosphere plays a role in driving ocean circulation at the surface and deep ocean through surface turbulent fluxes, it is imperative to understand the atmosphere's role on deep water formation and the strength of the GMOC. Numerical ocean models that consider atmospheric forcing often prescribe the atmospheric state with meteorological reanalysis data (Häkkinen 1999; Gulev et al. 2003; Bentsen et al. 2004; Bigg et al. 2005; Brodeau et al. 2010). Most reanalyses are global products that provide atmospheric information at a consistent time interval for at least 10 years (e.g., ERA-40, Simmons and Gibson 2000; JRA-25, Onogi et al. 2007). To force the ocean realistically in an air-sea coupled ocean circulation model, the surface turbulent fluxes prescribed must be accurate. In the Nordic Seas, inaccuracies in capturing the intensity of all atmospheric storms within the region will affect ocean forcing—more specifically, prescribing surface turbulent fluxes that are weaker than in reality due to a failure to capture all systems accurately will lead to underforcing of the ocean. In situ observations have been compared with atmospheric reanalysis data sets in the past, and such comparisons have suggested that reanalyses often underestimate near-surface wind speeds (Kelly et al. 1999; Chelton and Freilich 2005), which would lead to surface turbulent fluxes that are weaker than reality.

In order to improve the accuracy of wind fields and surface turbulent fluxes prescribed for an ocean model, the inclusion of small-scale and high-frequency phenomena within the boundary layer has been considered in past research. In simulating the tropical Pacific Ocean variability during the onset phase of El Niño during 1997/1998, Chen et al. (1999) found that their model compared favorably with observations when applying high-resolution wind forcing. Cardona and

Bracco (2012) concluded that including higher-frequency wind data impacts model representation of vertical transport in mesoscale eddies of the South China Sea, as vertical transport increases in tandem with increased temporal resolution. Vertical velocity in model runs forced with 6-hourly winds was approximately doubled in magnitude compared to model runs using daily-averaged winds, and a twelve-fold magnitude difference was seen compared to monthly-averaged winds. Using a coupled air-sea numerical model, Pickart et al. (2003) investigated deep convection over the Irminger Sea forced by a low-level Greenland tip jet that periodically manifests on the leeward side of Greenland. Because the Greenland tip jet is narrow and near the same meridional scale as the NCEP (National Centers for Environmental Prediction) reanalyses, it is not represented in the data and leads to underestimated wind speeds and surface turbulent fluxes.

Polar mesocyclones are high-latitude maritime systems that exist on the scale of 50 – 1000 km diameter (most in the northeast Atlantic are between 100 km and 500 km in size; Harold et al. 1999) and persist for short periods of time (3 – 36 h). They are typically associated with near-surface winds approaching or exceeding gale force, considerable momentum fluxes, and increased heat fluxes. Harold et al. (1999) suggested that mesoscale vortices tend to occur within the Nordic Seas—a key region for climatologically important deep water convection. The collective effect of these mesocyclones on vertical stratification within the ocean may influence convective timing and intensity. For ocean modelers attempting to capture the convective timing and intensity in the Nordic Seas accurately, it follows that polar mesocyclones in the region should be represented as accurately as possible when prescribing the atmospheric state.

Due to the spatiotemporal scale and domain of most polar mesocyclones, reanalysis data may be unable to capture or represent smaller and shorter-lived storms. The simplest reason for a data set to fail in resolving a storm is its grid coarseness and low temporal frequency. Additionally,

the remote locations in which many polar mesocyclones exist are beyond the reach of most surface-based synoptic observation networks, which complicates storm data assimilation into a reanalysis data set. Assimilating arctic observations within a regional assimilation system may improve the representation of arctic mesoscale phenomena (Renfrew et al. 2008; Moore 2012).

Using the European Centre for Medium-Range Weather Forecasts' atmospheric Reanalysis data (ERA-40), Condron et al. (2006) employed a cyclone detection algorithm to locate polar mesocyclones in mean sea-level pressure over a two year period in the northeast Atlantic, and compared the position of each detected cyclone with Harold et al.'s (1999) Advanced Very High Resolution Radiometer (AVHRR) data set of polar mesocyclones in the region. A majority (approximately 70 – 80%) of polar mesocyclones with a diameter of at least 500 km were detected in the ERA-40 mean sea-level pressure field. An almost linear decrease in storm detection was reported for systems smaller than 500 km in diameter—less than 20% of sub-250 km cloud systems found by Harold et al. (1999) were paired with a detected cyclone in ERA-40. Approximately 75% of northeast Atlantic polar mesocyclones recorded using AVHRR satellite data were smaller than 500 km in diameter. With such a large portion of storms unaccounted for in the ERA-40 mean sea-level pressure, Condron et al. (2006) concluded that the reanalysis data set is unreliable in representing sub-500 km diameter polar mesocyclones. The authors surmised that, as a consequence of a deficiency in detection via mean sea-level pressure, a considerable portion of surface turbulent fluxes linked to polar mesocyclones will be missed when forcing ocean models with ERA-40 (this conclusion is confirmed in Condron et al. 2008).

Following the aforementioned findings and implications, this research will analyze surface turbulent fluxes (momentum, sensible heat, and latent heat) associated with northeast Atlantic polar mesocyclones of variable size in the newly-developed Arctic System Reanalysis (ASRv1)

(Bromwich et al. 2010). The research will investigate the potential usefulness of supplementing a coupled air-sea ocean model with ASRv1 surface turbulent flux data. The research will include examinations of a polar mesocyclone on the upper end of the spatial scale to address potential system representation issues independent of the reanalysis' resolution, and smaller-scale storms to investigate problems regarding resolution. The analysis of ASRv1 that follows will be compared with results from a high spatiotemporal resolution atmospheric model—which is intended to be a substitute for an ideal data set or surface observations—as well as a commonly-used global reanalysis for completeness. Section 2 will detail the methods employed as well as data and model specifics. Section 3 will provide research results and findings, and the fourth section will offer conclusions and a discussion of the results.

CHAPTER TWO

METHODOLOGY AND DATA

Momentum fluxes, sensible heat fluxes, latent heat fluxes, and 10 m wind speeds associated with three polar mesoscale systems of variable size were analyzed over the northeast Atlantic. Analytic results from the Weather Research and Forecasting (WRF) model (Skamarock et al. 2008) and the Arctic System Reanalysis data set (ASRv1) are compared.

2.1. Research Domains

Two separate model runs were completed to analyze the three mesoscale systems. One polar mesocyclone with an approximate 700 – 800 km maximum diameter (size determined as in Harold et al. 1999) is simulated over the Barents Sea from 0000 UTC 17 December to 1200 UTC 21 December 2002 (Fig. 1). This first simulated system fits Rasmussen and Turner's (2003) polar low classification and was previously modeled by Føre et al. (2012). Though the domain of this storm is just outside of the Nordic Seas region, it is analyzed due to its size, proximity to the Nordic Seas, and its relation to the central objective of this research that encompasses polar mesocyclones in general.

The second simulation includes two systems of contrasting size between 0600 UTC 9 December to 0000 UTC 13 December 2006 (Fig. 2). Available AVHRR imagery (Fig. 2a) suggests two cyclonic cloud signatures at 0950 UTC 12 December 2006 off the Norwegian coast. One storm is approximately 550 km in maximum diameter and situated between Iceland and Norway for most of its lifetime. A smaller storm (approximately 250 – 300 km in diameter) is south-

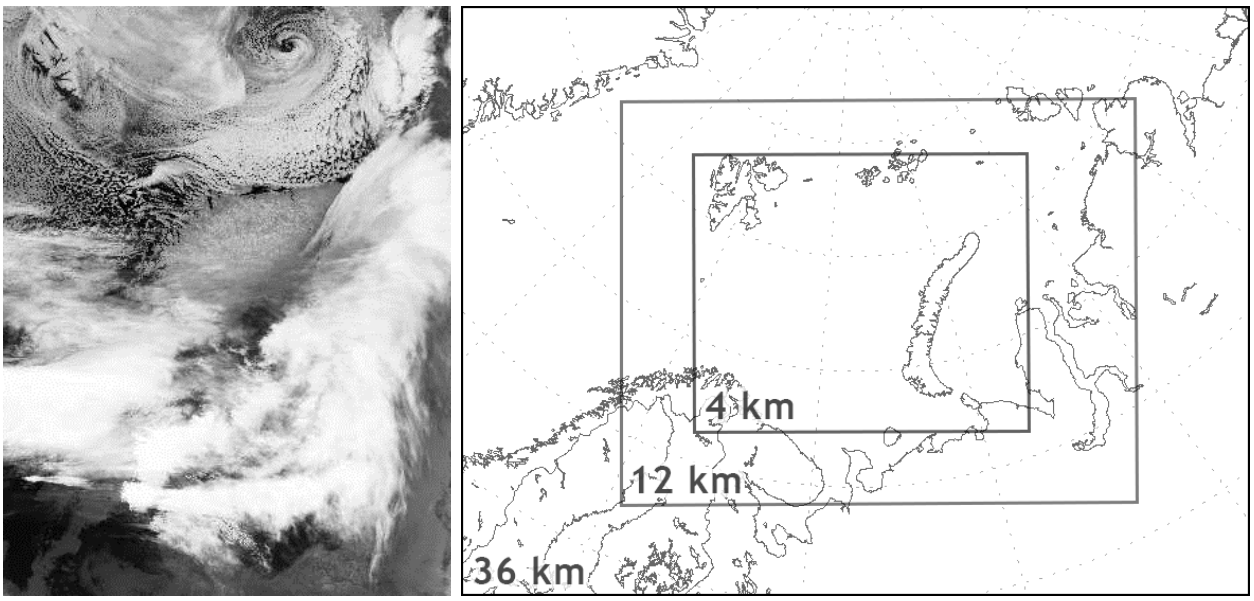

Fig. 1. (left) AVHRR channel 5 satellite image taken at 1017 UTC 19 December 2002, with a "hurricane-like" polar low visible at the top of the image, east of the Svalbard archipelago. (AVHRR images courtesy of the NERC Satellite Receiving Station at the University of Dundee, Dundee, United Kingdom.) (right) WRF model domain setup run from 0000 UTC 17 December to 1200 UTC 21 December 2002 for the storm pictured. Domain boundaries are drawn with respective grid spacing for each domain shown within each box.

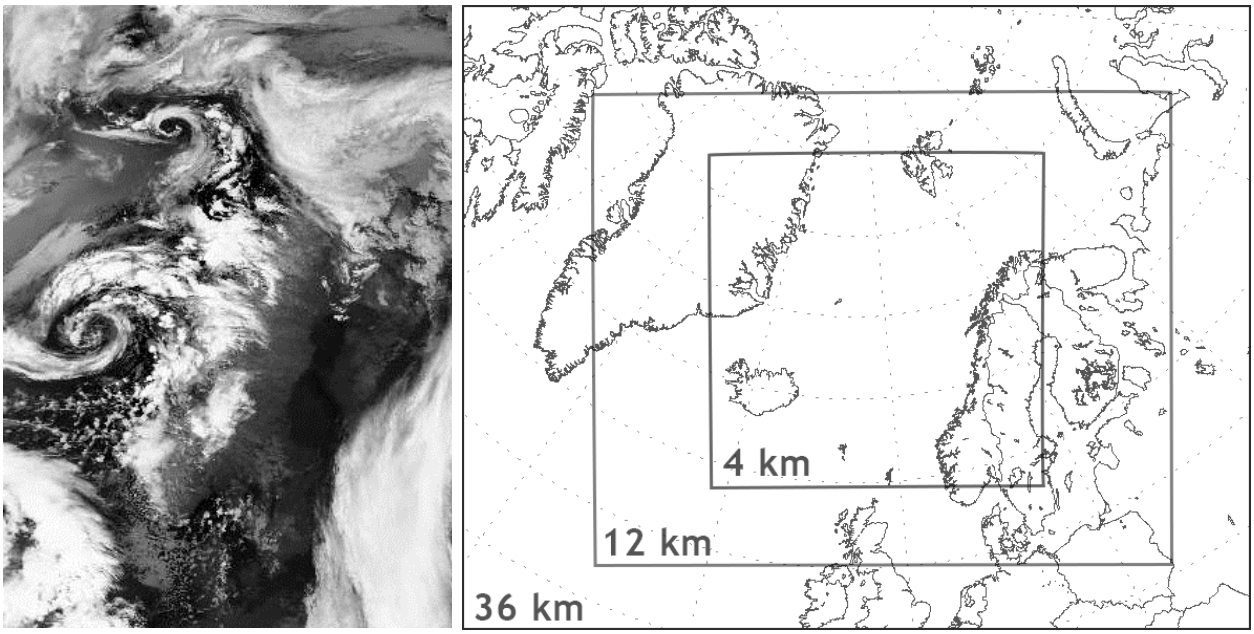

Fig. 2. (left) AVHRR channel 5 satellite image taken at 0950 UTC 12 December 2006, showing three polar mesocyclones off the coast of Norway. (right) WRF model domains for the run from 0600 UTC 9 December to 0000 UTC 13 December 2006 for the storms pictured. Domains are drawn as in Fig. 1b.

southwest of the Svalbard archipelago. Further examination using QuikSCAT data (version 3; Fore et al. 2014) suggests another signature to the west (approximately 200 – 250 km diameter).

2.2. WRF Model

The Weather Research and Forecasting model (WRF; Skamarock et al. 2008) is a state-of-the-art mesoscale numerical weather-prediction system often used in operational forecasting and meteorological research. In this research, version 3.5 of the WRF model was employed to simulate the atmospheric state over the regions indicated in Figs. 1b and 2b. WRF model characteristics are listed in Table 1 below. Conditions within the outermost domains were simulated with 36 km grid spacing, and the grid spacing for the intermediate and innermost domains were 12 km and 4 km, respectively. One-way nesting (i.e., parent to child nest only) was used in all model runs. Initial and boundary conditions were supplied to the model from the European Centre for Medium-Range Weather Forecasts' (ECMWF) ERA-Interim reanalyses with 0.75° × 0.75° grid spacing (Dee et al. 2011). Grid nudging for free-atmospheric horizontal wind, temperature, and water vapor was used in the outermost domain to maintain consistency between large-scale simulated features and the input data over time. Grid nudging was turned off after 72 h of runtime. All model runs used 51 vertical levels up to a model top of 10 hPa and had an increased vertical resolution near the surface (23 vertical levels below 850 hPa) to simulate processes more effectively within the planetary boundary layer, toward which polar-low tracks can be sensitive (Claud et al. 2004) and are crucial for modeling near-surface conditions. Positive-definite advection of meteorological parameters was utilized.

The new Kain-Fritsch (Kain 2004) cumulus parameterization scheme was applied to all but the innermost domain, which used no parameterization due to its high resolution allowing

convection to be explicitly resolved (Gentry and Lackmann 2010). Thompson's new double-moment bulk microphysics scheme (Thompson et al. 2008) and the Yonsei University (YSU) planetary boundary layer scheme with non-local closure (Hong et al. 2006) were used throughout all domains. The Rapid Radiative Transfer Model for General Circulation Models (RRTMG; Iacono et al. 2008) longwave and Goddard shortwave (Chou and Suarez 1994) schemes were implemented. The MM5 similarity surface scheme (Paulson 1970; Dyer and Hicks 1970; Webb 1970; Zhang and Anthes 1982; Beljaars 1994) was used in conjunction with the Unified NOAH Land Surface model option (Tewari et al. 2004). Sea surface temperatures (SSTs) and sea-ice flags throughout model simulations are always equal to those at the initialization time.

2.3. Model Verification

Wind data were taken from NASA's QuikSCAT scatterometry data set (version 3; Fore et al. 2014), which provides level 2 information in swaths and has a grid spacing of 12.5 km × 12.5 km. Backscattered power resulting from the roughness of the ocean surface is detected by a scatterometer, which is used to infer winds at a reference height assuming a neutrally stratified atmosphere (Liu 2002). These inferred winds are called *equivalent neutral winds*. The equivalent neutral wind data is compared with simulated 10 m wind vectors to determine the model's accuracy in representing this crucial field. A data swath is provided approximately every 1.7 h from 27 October 1999 to 22 November 2009. The time coverage limited the storms available for analysis. The availability of swath data for a region covering particular storms had to be considered before analysis could be conducted, further limiting analysis possibilities. All data were taken directly from NASA's publically-accessible Physical Oceanography Distributed Active Archive Center (PODAAC, http://podaac.jpl.nasa.gov/).

2.4. Reanalysis Data

The Arctic System Reanalysis version 1 (ASRv1) data set combines modeling and observations to construct air-sea and ice-land surface system descriptions of the Arctic region (domain shown in Fig. 3) every 3 h from the start of 2000 to the end of 2012. The forecast model used in ASRv1 is the Polar WRF: an adaptation of the WRF model version 3.3.1 specifically designed for polar environments (Hines and Bromwich 2008; Bromwich et al. 2009; Hines et al. 2011). The Polar WRF model uses the staggered Arakawa grid-C with 361 × 361 grid points and 30 km × 30 km grid spacing on a latitude-longitude plane. Polar WRF uses terrain-following, dry hydrostatic-pressure vertical coordinates with 71 vertical levels and a model top of 10 hPa. More than 25 of the 71 vertical levels are packed below 850 hPa, with the lowest model level at 8 m

Table 1. Characteristic details of the WRF model employed and ASRv1.

Characteristic	Wrf Model	ASRv1
Model	WRF version 3.5	Polar WRF version 3.3.1 coupled to NOAH Land Surface Model
Dynamical core	Non-hydrostatic, Eulerian, fully compressible	Non-hydrostatic, Eulerian, fully compressible
Lateral boundary conditions	ERA-Interim	ERA-Interim
Horizontal resolution	36 km outer domain, 12 km intermediate domain, 4 km inner domain	90 km outer domain, 30 km inner domain
Nesting behavior	One-way nesting (downscale only)	One-way nesting (downscale only)
Horizontal grid type	Arakawa C-Grid staggering	Arakawa C-Grid staggering
Vertical resolution	51 vertical levels, 10 hPa model top	71 vertical levels, 10 hPa model top
Time-integration scheme	Third-order Runge-Kutta	Third-order Runge-Kutta
Sea surface temperature	ERA-Interim, constant from initialization	ERA-Intertim, time-variable
Sea-ice	ERA-Interim sea-ice cover, constant from initialization	Time-variable with concentration and thickness from SSMI and AMSRE data, annually varying albedo, and seasonally varying snow cover
Land surface	Unified NOAH Land Surface Model	High Resolution Land Data Assimilation System (HRLDAS; Chen et al. 2007) with NOAH Land Surface Model
Planetary boundary layer	Yonsei University (YSU)	Mellor-Yamada-Nakanishi-Niino (MYNN) (Nakanishi 2001; Nakanishi and Niino 2004; Nakanishi and Niino 2006) 2.5-level scheme
Radiation	RRTMG longwave and Goddard shortwave schemes.	RRTMG longwave and shortwave schemes
Microphysics	Thompson double-moment bulk scheme	Goddard (Tao and Simpson 1993; Tao et al. 2003)
Cumulus parameterization	None in the 4 km inner domain; New Kain-Fritsch otherwise	Kain-Fritsch (Kain and Fritsch 1990; Kain and Fritsch 1993)

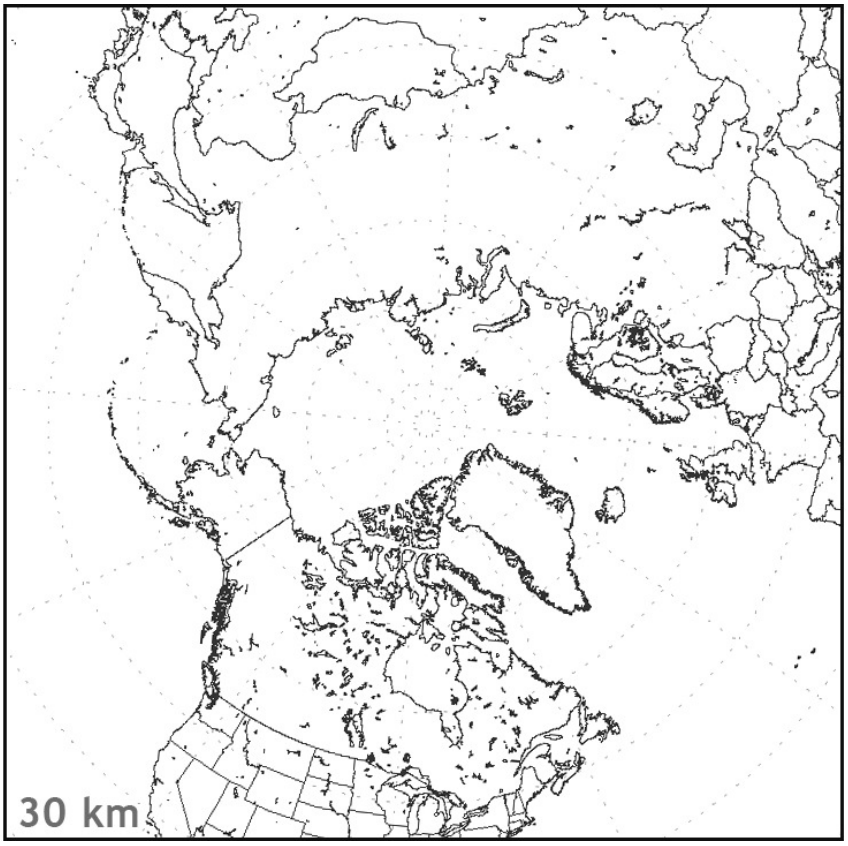

Fig. 3. ASRv1 30 km resolution product domain centered over 90°N. Reanalyses are available every 3 h.

above the surface. Polar WRF utilizes an improved NOAH Land Surface model that includes fractional sea ice and additional sea-ice characteristics, such as thickness, snow cover on sea ice, and albedo. ASRv1 assimilates atmospheric observations from conventional observations from ships, buoys, radiosondes, and METARs; as well as satellite observations and radiance information. Bromwich et al. (2015) explain extensively Polar WRF model parameterizations and specifics, and detail the data assimilation techniques employed for ASRv1. A summary of the reanalysis' characteristics is provided in Table 1.

Displays of 6-hourly averaged surface turbulent fluxes from the National Centers for Environmental Prediction's (NCEP) Climate Forecast System Reanalysis (CFSR; Saha et al. 2006)

also are provided for completeness. The CFSR dataset includes surface turbulent fluxes with a 0.312° × ~0.312° grid spacing. CFSR data can be used to prescribe the atmospheric state in an ocean model, and its information is included to illustrate differences between the arctic-specific ASRv1 dataset and CFSR's global dataset. From such comparisons, the possible impacts of assimilating ASRv1 information into a model instead of CFSR data (for example) are investigated.

CHAPTER THREE

RESULTS

The near-surface winds from WRF Model results and ASRv1 are investigated first. Since the wind profile close to water surfaces influences the fluxes, an examination of 10 m wind speeds provides insight regarding its impact on flux calculations. A thorough analysis of surface turbulent fluxes follows. The analyses include spatial plots and distributions of fluxes. Domains for the spatial plots are chosen and intended to encapsulate storms entirely throughout their lifetime, while limiting excess area surrounding the storms (to reduce inclusion of that data in distributions). Three cases will be examined: a hurricane-like December 2002 polar low, a December 2006 polar low, and a pair of polar mesocyclones in December 2006.

3.1. Near-surface Wind Vectors

3.1.1. December 2002 Polar Low

The polar low located west of Novaya Zemlya (islands north of Russia) from 18 – 20 December 2002 developed an impressive, tropical cyclone-like structure complete with spiral cloud bands, a clear eye and warm core, and horizontal axisymmetry that was readily visible from satellite imagery (Fig. 1a). Føre et al. (2012) modeled and analyzed "hurricane-like" heat fluxes associated with this storm. Baroclinicity and upper-level potential vorticity forcing drove a deepening phase that allowed the polar low to develop an approximate central pressure of 960 hPa.

The storm's center developed a clear, calm eye with an eyewall. Wind speeds at 10 m from the WRF simulation and ASRv1 data (Fig. 4) are strongest around the calm center of the storm, with maximum winds exceeding 25 m s^{-1} in WRF, and maximum winds greater than 20 m s^{-1} in

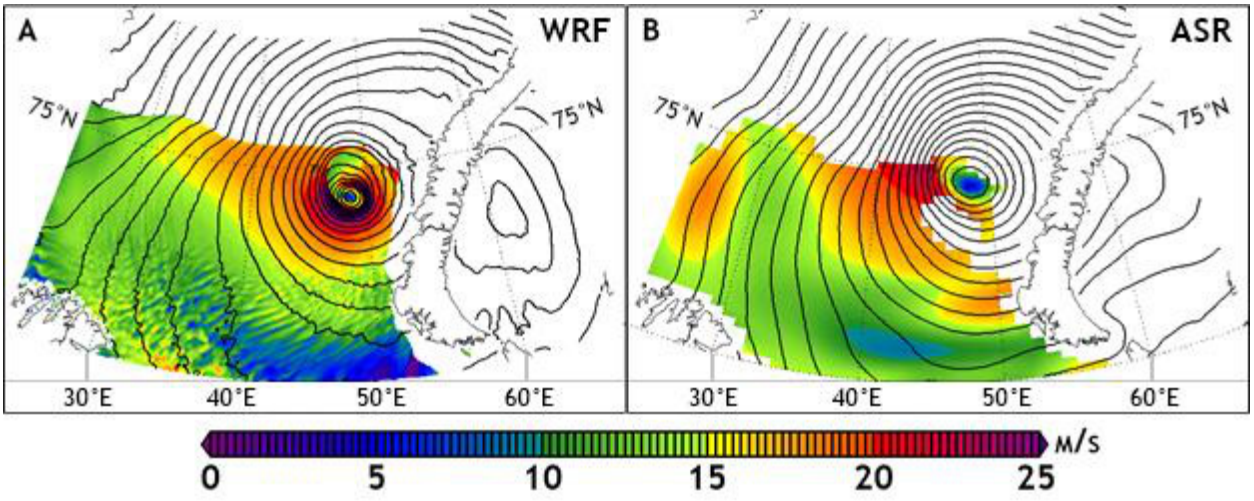

Fig. 4. Shaded 10 m horizontal wind speeds for the innermost domain about the December 2002 polar low (24°E – 67°E, 70°N – 78°N). (a) WRF simulation winds with overlaid contours of surface pressure (1 hPa interval, ~955 hPa minimum) at 0600 UTC 19 December 2002. (b) ASRv1 winds with contoured mean sea-level pressure (1 hPa interval, ~960 hPa minimum) from 0600 UTC 19 December 2002. The polar low at this time is near peak intensity as it recurves westward near Novaya Zemlya. Wind data are masked out over sea ice and land, and pressure contours are masked out over land.

ASRv1. While the 10 m wind fields in the environment about the storm generally appear similar between the WRF simulation and ASRv1, the WRF simulation produced a stronger maximum 10 m wind speed than ASRv1 throughout the polar low's lifetime. The maximum near-surface winds in the WRF simulation are located within the eyewall. Strong near-surface wind speeds in ASRv1 encompass a broader area about a calm center of rotation. While the WRF model's stronger 10 m winds cover less area than ASRv1, the simulation's greater wind maximum implies a stronger wind shear near the surface, thus affecting surface turbulent fluxes.

QuikSCAT swath data of the storm at 1603 UTC 19 December 2002 provide the 10 m equivalent neutral wind field (Fig. 5). Winds from the QuikSCAT product and the WRF simulation at 1600 UTC 19 December 2002 generally agree with the polar low's position and strength. The swath of gale force winds to the west of the storm is visible in both the model and the scatterometry data, and both depict the storm with maximum sustained winds exceeding 20 m s^{-1} (the threshold for reliable QuikSCAT wind speed measurements, according to the product

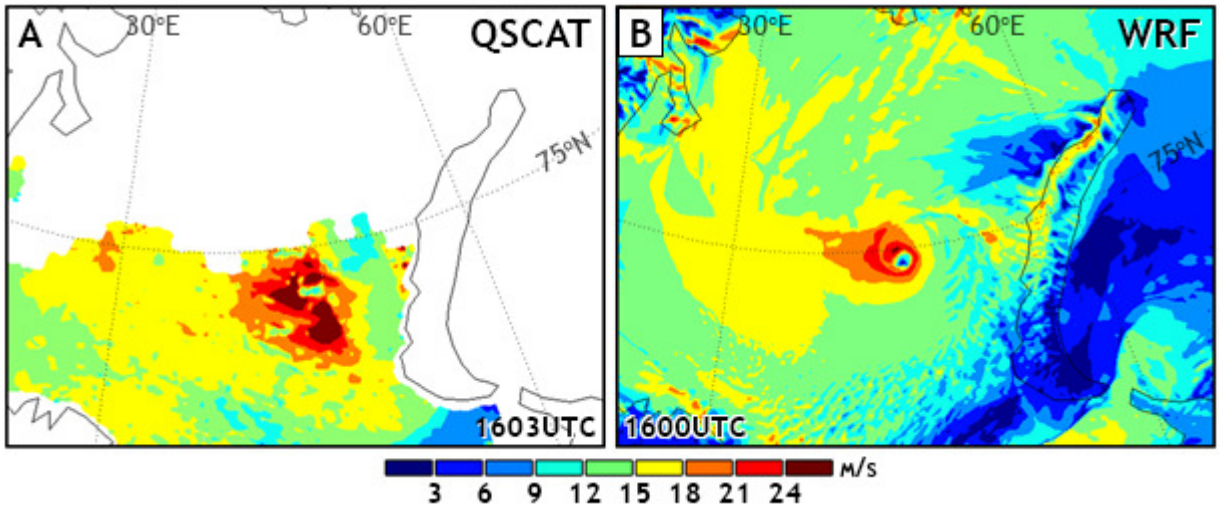

Fig. 5. (a) QuikSCAT 10 m equivalent neutral wind speeds (m s^{-1}) from swath data at 1603 UTC 19 December 2002. (b) WRF model simulated 10 m wind speeds (m s^{-1}) at 1600 UTC 19 December 2002. Wind data over ice and near land has been removed in QuikSCAT.

description) and a calm eye. The area of wind speeds stronger than 12 m s^{-1} south and southwest of the polar low appears larger in QuikSCAT than the model simulation.

The similarities between ASRv1 and the WRF simulation outside of the resolution-based discrepancies (i.e., WRF simulation's small-scale amplifications in the wind) suggest that sizable differences in fluxes resulting from the near-surface wind can be attributed to ASRv1's resolution. The near-surface wind profile accuracy is especially important in calculating momentum flux. Heat fluxes also are dependent on the near-surface wind profile; however, heat fluxes are also dependent on other near-surface profiles (e.g., temperature and moisture).

3.1.2. December 2006 Polar Low

A weaker, smaller spiraliform polar low that travelled along Norway's coastline on 12 December 2006 did not develop the "hurricane-like" features present in the December 2002 storm. Once again, the WRF simulations of this polar low depicted stronger 10 m wind speeds than the

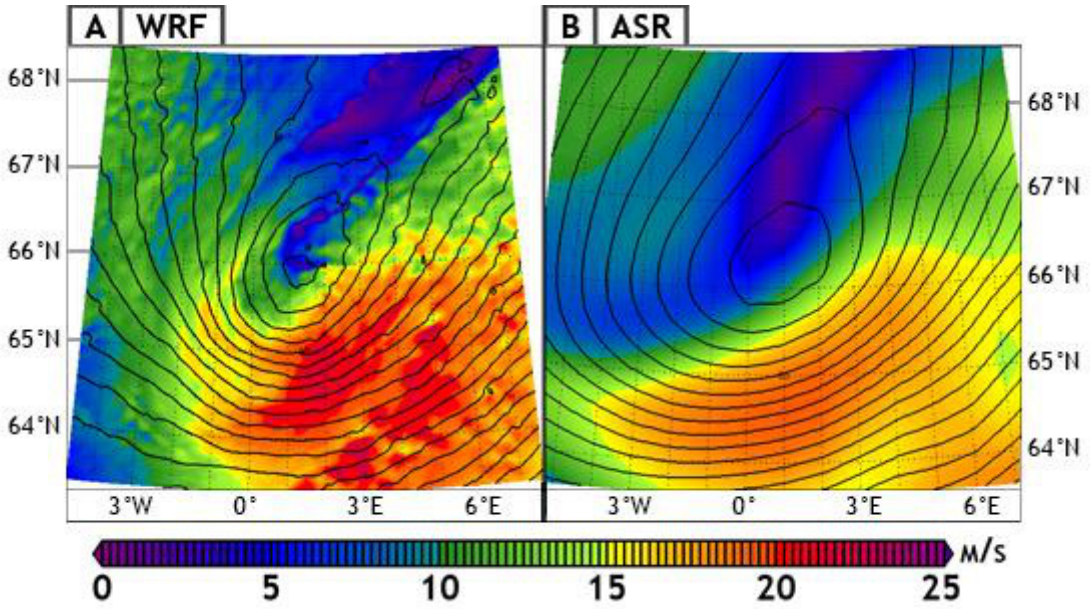

Fig. 6. Shaded 10 m wind speeds from the December 2006 polar low. The domain is positioned over the storm's minimum pressure with ~550 km width and length at the center of the domain. (a) WRF simulated winds and contoured surface pressure (1 hPa interval, ~963 hPa minimum) at 0900 UTC 12 December 2006. (b) ASRv1 wind data with contoured mean sea-level pressure (1 hPa interval, ~964 hPa minimum) at 0900 UTC 12 December 2006. The polar low travels north-northeastward, east of Norway. In the WRF simulation, there appear to be areas of increased wind speed in the swath of wind speeds greater than 15 m s^{-1} when compared to ASRv1.

ASRv1 data south of the storm's center (Fig. 6), with the strongest winds exceeding 20 m s^{-1}. However, the spatial distribution and pattern of wind speeds about the storm is mostly similar throughout the storm's lifetime. The strongest wind swath in both sets of data is oriented along the southeastern portion of the storm's center. Weaker winds (~5 m s^{-1}) persisted north of the calm and open storm center. Both the WRF simulation and ASRv1 data suggest the storm developed a 963 hPa central pressure, approximately, around 0900 UTC 12 December 2006. As the polar low advanced north-northeastward away from Iceland and along the coast of Norway, it began to dissipate. The WRF simulation depicts the storm impacting the northern coast of Norway at 2100 UTC 12 December 2006, while ASRv1 sees the storm vanish over the open water just northwest of Norway during the early hours of 13 December 2006 (not shown).

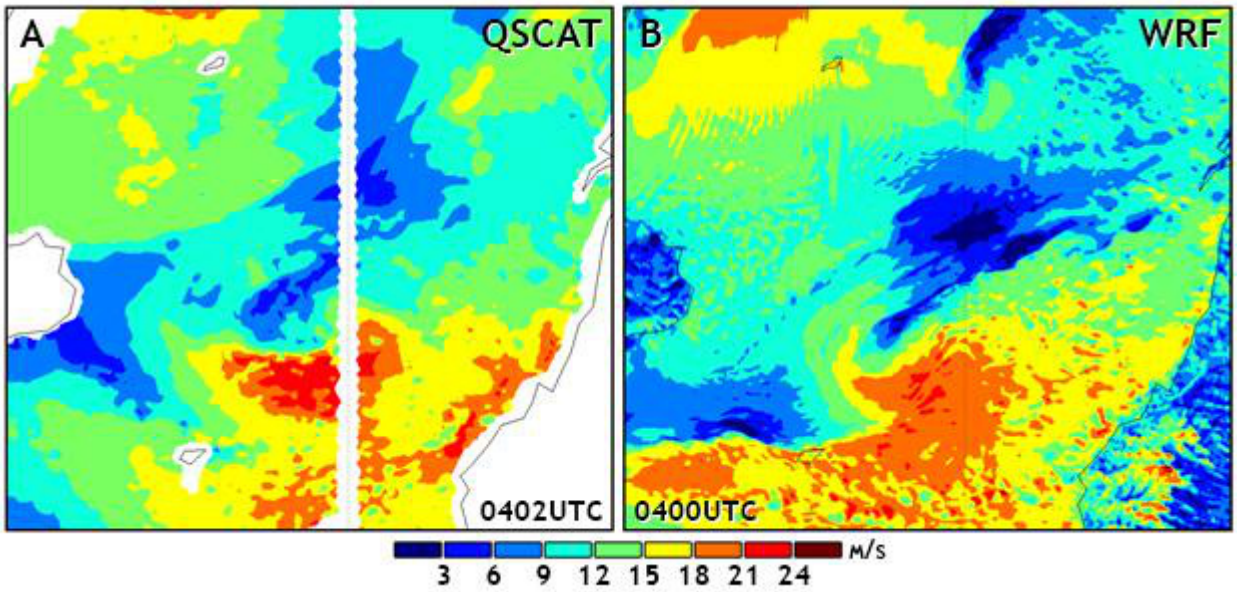

Fig. 7. (a) QuikSCAT 10 m equivalent neutral wind speeds (m s^{-1}) from swath data at 0402 UTC 12 December 2006, with a focus on the polar low east-northeast of Iceland. (b) WRF model simulated 10 m wind speeds (m s^{-1}) at 0400 UTC 12 December 2006. Wind data near land and 0° longitude has been removed in QuikSCAT data.

QuikSCAT ocean winds data encompassed the polar low at 0402 UTC 12 December 2006 (Fig. 7). The 10 m equivalent neutral wind field is compared against the WRF simulation at 0400 UTC 12 December 2006. Both datasets suggest that the winds south of the storm's center are strongest, exceeding 18 m s^{-1}. QuikSCAT winds on the north side of the storm are ~ 6 – 12 m s^{-1}, with the simulation calculating even weaker winds in the area (~ 3 – 6 m s^{-1}).

The WRF simulation and ASRv1 differ in the storm's location and the 10 m wind speeds to the west of the storm, where wind speeds are slightly stronger in the WRF simulation than ASRv1. The 10 m wind speeds are also stronger south of the storm in the WRF simulation, but it appears that the difference in resolution may be responsible for the difference in 10 m wind speeds in this area. The wave-like amplifications of WRF simulated 10 m wind speed south of the storm are likely too small in size for ASRv1 to resolve.

3.1.3. December 2006 Sub-350 km Polar Mesocyclones

The AVHRR satellite imagery available at 0950 UTC 12 December 2006 (Fig. 2) indicate two cyclonic signatures at first glance: a polar low east of Iceland—discussed in the previous subsection—and a smaller polar mesocyclone south of Svalbard archipelago. Upon closer examination, a less-defined third cyclonic signature appears to be present west of the northernmost polar mesocyclone.

Compared to the previous cases, there is less agreement between the WRF simulation and ASRv1 representing these smaller-scale mesocyclones. The surface analysis at 0900 UTC 12 December 2006 (Fig. 8) reveals notable discrepancies between the WRF experiment and ASRv1: The model (Fig. 8a) simulates three low pressure centers that are separated from one another by approximately 2 hPa, while ASRv1 (Fig. 8b) depicts a single elongated low. In the WRF simulation, strong north-northwesterly 10 m winds (> 15 m s^{-1}) near sea ice off the coast of Greenland produce an isolated outbreak of cold air; while ASRv1 10 m winds are calmer in that region (~10 m s^{-1}). In close proximity to the three mesocyclones from the WRF simulation are small regions of enhanced near-surface wind speeds exceeding 15 m s^{-1}. The one mesocyclone present in ASRv1 at 0900 UTC 12 December 2006 appears to have a maximum 10 m wind speed no greater than 15 m s^{-1}; however, an area of 10 m winds greater than 10 m s^{-1} is present along the north side of the storm, which is absent in the WRF simulation.

The QuikSCAT swath data from 0402 UTC 12 December 2006 (Fig. 9a) suggest that only two polar mesocyclones exist at this time, while the WRF model simulates three mesocyclones at 0400 UTC 12 December 2006 (the extra in the southwest corner of the domain; Fig. 9b). In general, the winds around this system are weaker in the WRF simulation than in QuikSCAT, with the

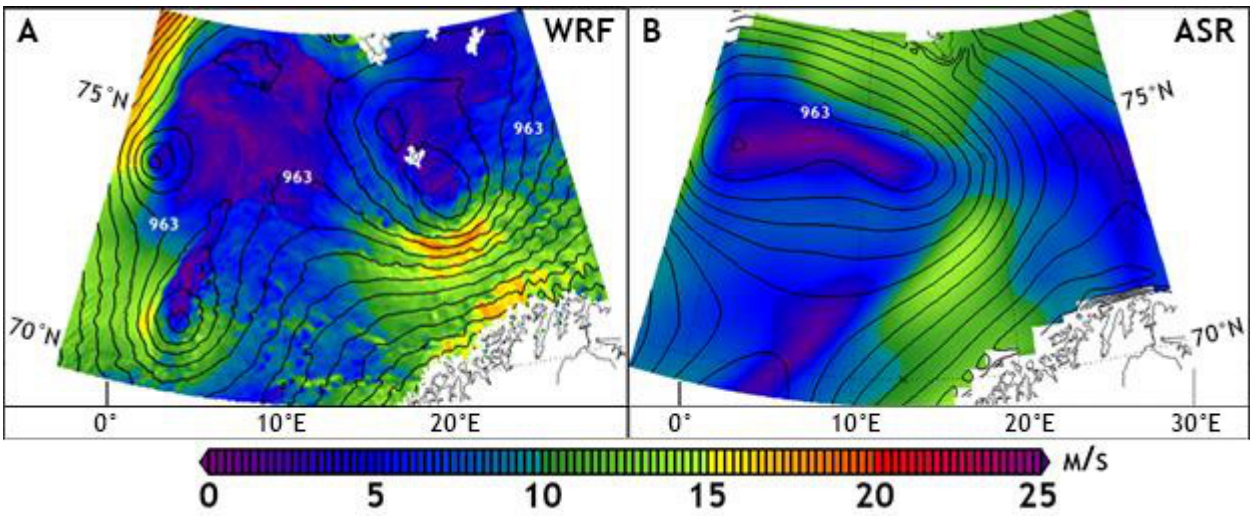

Fig. 8. Shaded 10 m horizontal wind speeds about the smaller polar mesocyclones north of the December 2006 polar low (3°W – 30°E, 69.5°N – 77°N). (a) WRF simulated winds with contoured surface pressure (1 hPa interval) at 0900 UTC 12 December 2006. (b) ASRv1 wind data and contoured mean sea-level pressure (1 hPa interval) at 0900 UTC 12 December 2006. The domain is situated just south of Svalbard archipelago and northwest of Norway. The 963 hPa contour is marked. Wind and pressure data are masked out over land.

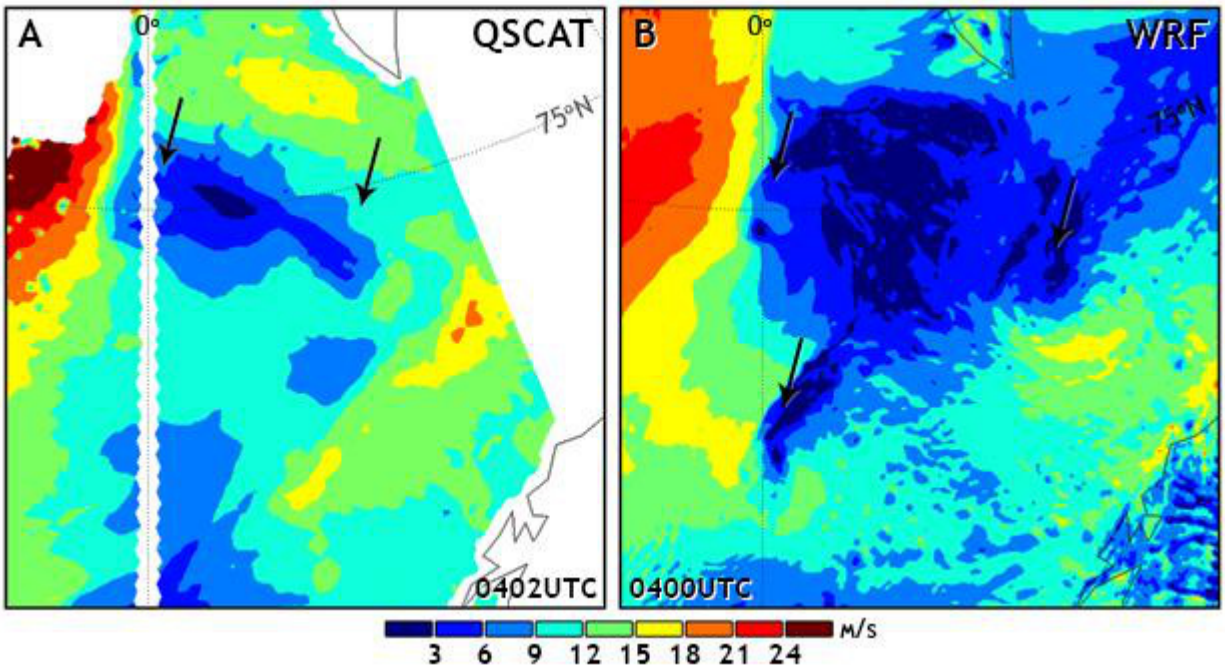

Fig. 9. (a) QuikSCAT 10 m equivalent neutral wind speeds (m s^{-1}) from swath data at 0402 UTC 12 December 2006, focusing on the polar mesocyclones south of Svalbard archipelago. (b) WRF model simulated 10 m wind speeds (m s^{-1}) at 0400 UTC 12 December 2006. Wind data near land, ice, and 0° longitude has been removed in QuikSCAT data. Cyclonic wind signatures are marked with black arrows.

simulation showing a much larger area of wind speeds less than 6 m s^{-1}.

Because the QuikSCAT information appears to disagree considerably with the WRF simulation on its depiction of the system, it would be difficult to defend the simulation results as a substitute for ground truth information of this system. The ASRv1 data seem more consistent with the satellite's illustration of the system than the WRF simulation, though the near-surface winds to the east-southeast of the system are weaker in ASRv1 than QuikSCAT implies via equivalent neutral wind data.

3.2. Momentum Flux

Momentum flux—or wind stress magnitude (hereafter simplified as *wind stress*)—is a vertical flux of horizontal momentum, expressed as a force per unit area (commonly N m^{-2}). The WRF surface schemes define momentum flux, τ :

(1) $$\tau = \rho u_* u_*$$

Equation 1 uses the product of air density, ρ, and the square of friction velocity, u_* . Spatial plots and distributions of momentum flux will be examined for the three cases. The data shown in spatial plots will be used to create distributions. Due to the movement of the December 2006 polar low, a ~ 550 km × 550 km moving domain will follow the storm with time, centered on its minimum sea-level pressure (which is different between the WRF simulation and ASRv1). The domains used for the December 2002 polar low and the December 2006 polar mesocyclones are static and shared between the WRF simulation and ASRv1.

3.2.1. December 2002 Polar Low

An examination of near-surface winds suggests that the "hurricane-like" polar low from 18 December to 20 December 2002 west of Novaya Zemlya (Fig. 4) should be associated with impressive wind stresses, especially coincident with its eyewall. Indeed, the momentum fluxes calculated in the WRF simulation exceed 2.5 N m^{-2} near the eye of the polar low (Fig. 10a) from 2100 UTC 18 December to 1200 UTC 19 December, and nearly 4 N m^{-2} at 0300 UTC 19 December (Fig. 11). Conversely, using ASRv1, the momentum fluxes never exceed 2.5 N m^{-2}. In addition, the extent of wind stresses stronger than 1.25 N m^{-2} in ASRv1 data appears to be greater than in the WRF simulation (Fig. 10b). The 6-hourly average of momentum flux in CFSR data (averaged from 0600 UTC to 1200 UTC 19 December; Fig. 10c) appears to capture the storm itself, but the wind stresses are much weaker (< 1.5 N m^{-2} throughout) than in ASRv1 and the WRF simulation.

Throughout most of the polar low's lifetime, the extreme values of momentum flux in the WRF simulation are greater than those in the ASRv1 data (Fig. 11). For several time periods, the maximum value of momentum flux in the WRF simulation is at least 0.5 N m^{-2} greater than the maximum in ASRv1. Despite these differences, the median, 25th percentile, and 75th percentile of wind stress distributions in the domain about the storm are often greater in the ASRv1 data than the WRF simulation. The WRF simulation produced weaker wind stresses in much of the area outside the region of intense momentum fluxes (about the eyewall) compared to ASRv1. Thus, the WRF model does not persistently simulate stronger wind stresses than ASRv1 throughout the domain, even though the maximum momentum fluxes are often greater in WRF. The differences in the maximum momentum fluxes are likely a result of ASRv1's coarser resolution not capturing the strongest momentum fluxes, which cover a small area as seen in Fig. 10a.

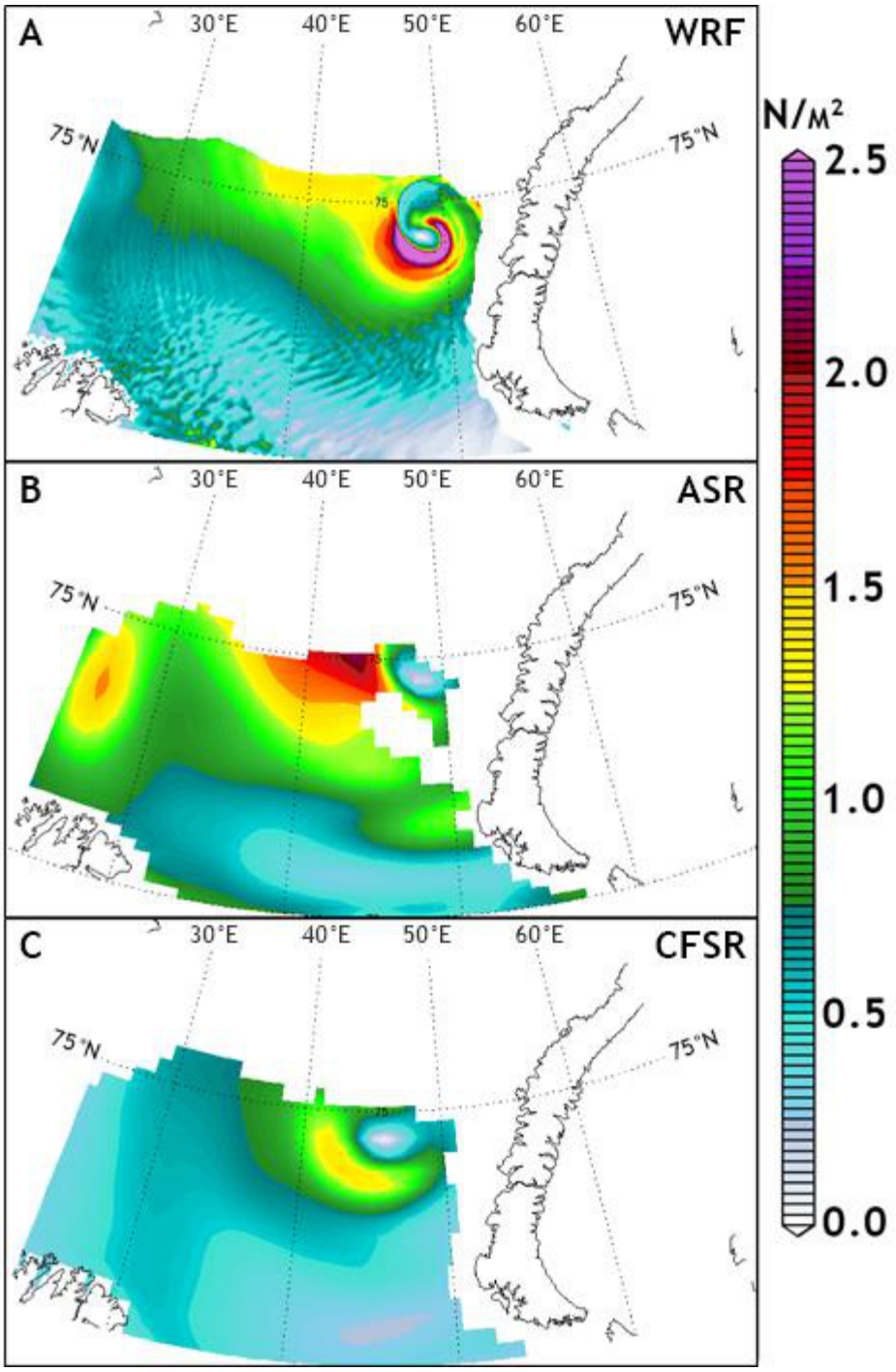

Fig. 10. (a) Shaded momentum flux (N m^{-2}) from a WRF simulation at 0600 UTC 19 December 2002. (b) Shaded momentum flux (N m^{-2}) in ASRv1 data at 0600 UTC 19 December 2002. (c) CFSR Shaded 6-hour average momentum flux (N m^{-2}), averaged from 0600 UTC to 1200 UTC 19 December 2002. Wind stress data are masked out over land and sea ice. At this time, a small area of intense wind stress greater than 2.5 N m^{-2} can be seen surrounding the polar low's eye in the WRF simulation. The distributions of the data in the domain are shown in Fig. 11.

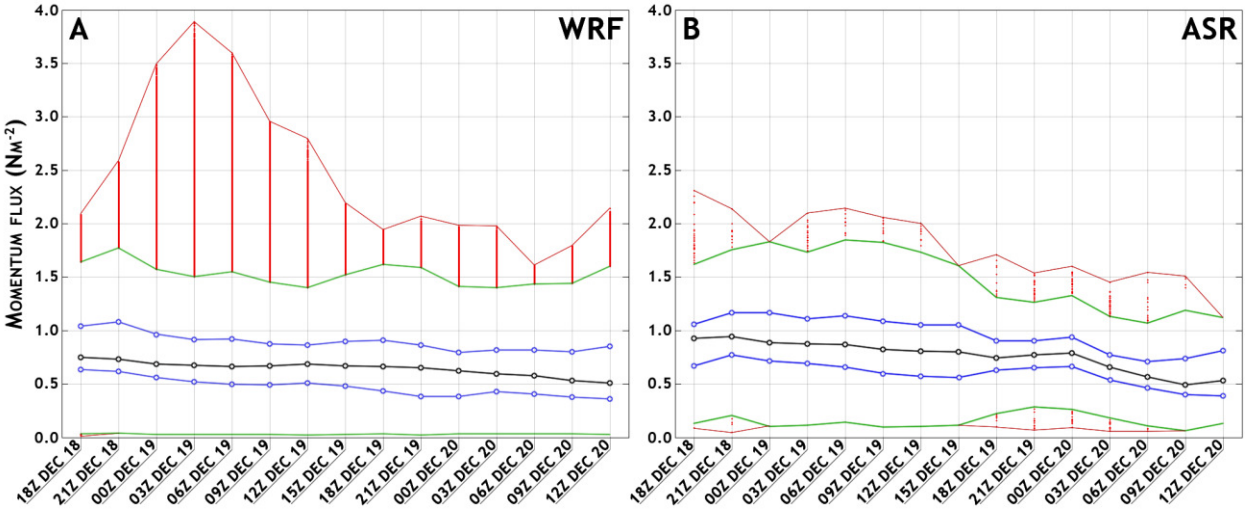

Fig. 11. Distributions of momentum flux (N m^{-2}) from (a) the WRF simulation and (b) ASRv1 during the lifetime of the December 2002 polar low. Data is taken from the domain shown in Fig. 10 (masked out data removed). Black lines mark the median of data in the area, and blue lines indicate the 25th and 75th percentiles (τ_{25} and τ_{75} respectively). Green lines demarcate the range of non-extreme values, where values between lines are less than $\tau_{75} + 1.5 \times (\tau_{75} - \tau_{25})$ and greater than $\tau_{25} - 1.5 \times (\tau_{75} - \tau_{25})$. Extreme data are red dots, with maxima and minima marked with red lines.

The most noticeable momentum flux differences between ASRv1 and the WRF simulation lie in the extreme values, which can be attributed to a difference in resolution. Otherwise, ASRv1 and the WRF simulation produce similar distributions of momentum flux. Both the WRF model and ASRv1 produce greater momentum fluxes than CFSR provides for this storm.

3.2.2. December 2006 Polar Low

The December 2006 polar low was not as strong or as large as the December 2002 storm, but Fig. 5 suggests that the storm did produce swaths of wind near or greater than gale force. The WRF simulation again produces a wider range of momentum fluxes around the storm that includes stronger extreme values over small areas (Fig. 12). The maximum wind stresses over time for the WRF simulation are often greater than 1.5 N m^{-2}, whereas momentum fluxes from ASRv1 never exceed 1.4 N m^{-2} (Fig. 13). Unlike the differences seen between the WRF simulation and ASRv1 in representing the December 2002 polar low (Fig. 11), the WRF simulation seems to produce

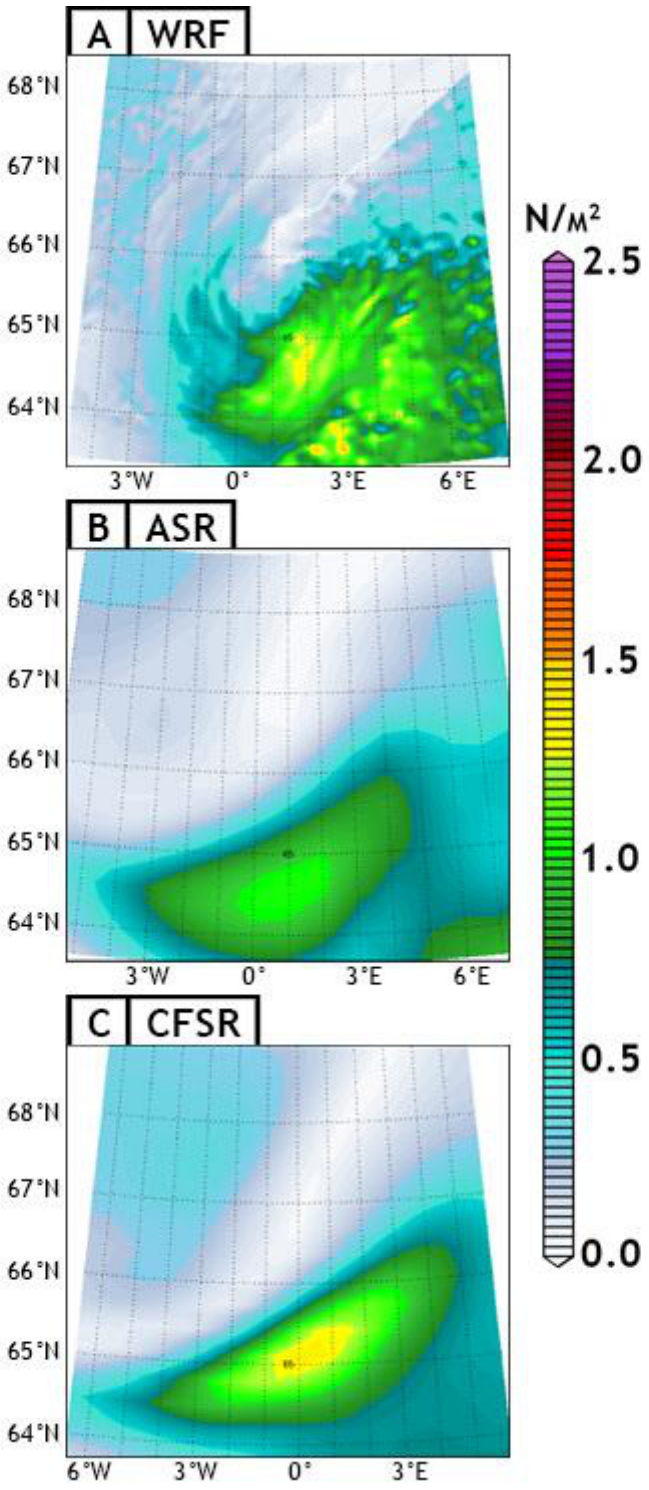

Fig. 12. (a) Shaded momentum flux (N m^{-2}) from a WRF simulation at 0900 UTC 12 December 2006. (b) Shaded momentum flux (N m^{-2}) in ASRv1 data at 0900 UTC 12 December 2006. (c) CFSR Shaded 6-hour average momentum flux (N m^{-2}), averaged from 0600 UTC to 1200 UTC 12 December 2006. The position of this domain changes with time, following the storm's minimum pressure.

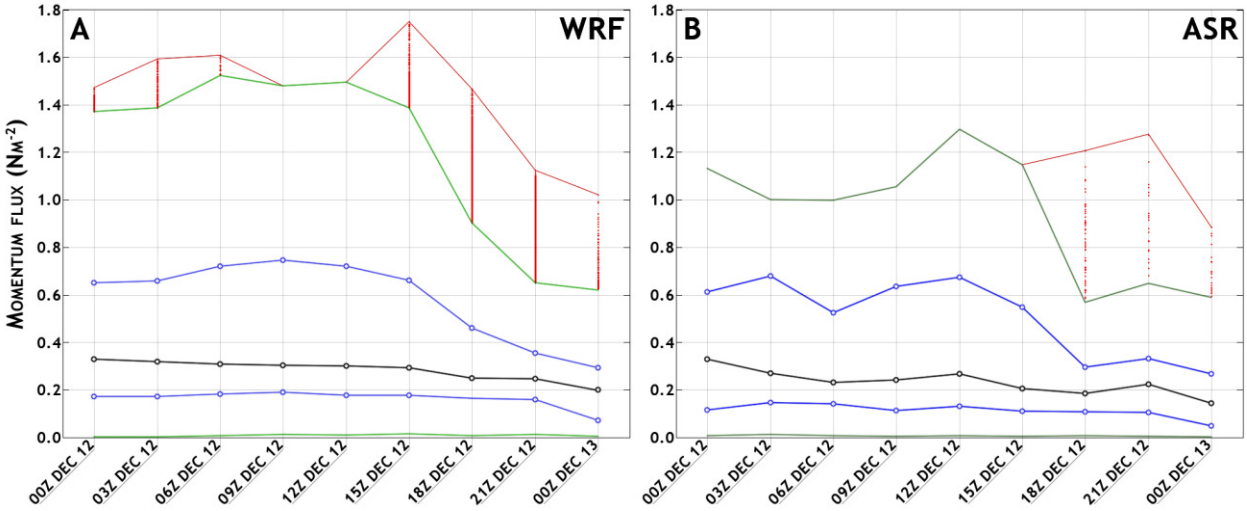

Fig. 13. Distributions of momentum flux (N m^{-2}) from (a) the WRF simulation and (b) ASRv1 for the December 2006 polar low. Black lines mark the median of data in the area, and blue lines indicate the 25th and 75th percentiles (τ_{25} and τ_{75} respectively). Green lines demarcate the range of non-extreme values, where values between lines are less than $\tau_{75} + 1.5 \times (\tau_{75} - \tau_{25})$ and greater than $\tau_{25} - 1.5 \times (\tau_{75} - \tau_{25})$. Extreme data are red dots, with maxima and minima marked with red lines.

distributions of momentum flux that are stronger than ASRv1. Both the upper and lower quartiles from WRF are almost always greater than those from ASRv1 (exception at 0300 UTC 12 December 2006). The 6-hour average momentum flux (0600 UTC to 1200 UTC 12 December) from CFSR shows a swath of increased wind stresses, the highest values of which are greater than 1.25 N m^{-2}.

The WRF simulation produces stronger momentum fluxes than the ASRv1 data throughout most of the lifetime of the polar low. The differences in maximum wind stress between the two sets of data are often between 0.2 N m^{-2} and 0.6 N m^{-2} (Fig. 13). Differences between lower and upper quartiles are usually around 0.1 N m^{-2} and no greater than 0.2 N m^{-2}. Since the WRF simulated wind stresses are often greater than those in ASRv1, there is the question of whether a data set is calculating wind stresses to be systematically stronger or weaker. Comparisons between ASRv1 and WRF simulated 10 m winds (Fig. 6) suggest that near-surface winds in WRF are often stronger; and QuikSCAT wind data (Fig. 7) appears to support WRF's stronger winds, which can

explain the persistent difference in wind stress between ASRv1 and WRF. Momentum flux also considers the air density near the surface, which also may be causing differences. The 6-hourly averaged CFSR (from 0600 UTC to 1200 UTC 12 December 2006) also produces stronger momentum fluxes than ASRv1 at 0900 UTC 12 December 2006. However, the difference between CFSR and ASRv1 may be due to the 6-hour averaging in CFSR, which would include information from near the polar low's peak intensity at 1200 UTC 12 December 2006 (Fig. 13).

3.2.3. December 2006 Sub-350 km Polar Mesocyclones

Analyzing the environment containing the set of polar mesocyclones north of the polar low reveals a cold-air outbreak off the edge of sea ice along Greenland's eastern coast. Because this research is not concerned with representing cold-air outbreaks, but is intended to focus on the polar mesocyclones, data west of the Greenwich meridian and north of 73.5°N is omitted (Fig. 14) from this analysis. Including these data near the cold-air outbreak otherwise affect the flux distributions to a large degree, particularly those data concerning heat fluxes.

The WRF simulation and ASRv1 data portray the system north of the December 2006 polar low differently, as seen in the analysis of the near-surface winds and pressure fields (Fig. 8). A view of the wind stresses (Fig. 14) echoes these differences. Generally, the wind stress field is weak across the WRF simulation, the ASRv1 dataset, and the CFSR 6-hourly average dataset. However, there are small-scale areas of increased wind stress seen in the WRF model results, as already seen in previous wind stress analyses. In the WRF simulation, the strongest momentum fluxes are persistently greater than 0.8 N m^{-2} and sometimes exceed 1.0 N m^{-2} (Fig. 15). The ASRv1 momentum fluxes are often less than 0.8 N m^{-2}. A majority of the wind stresses in the

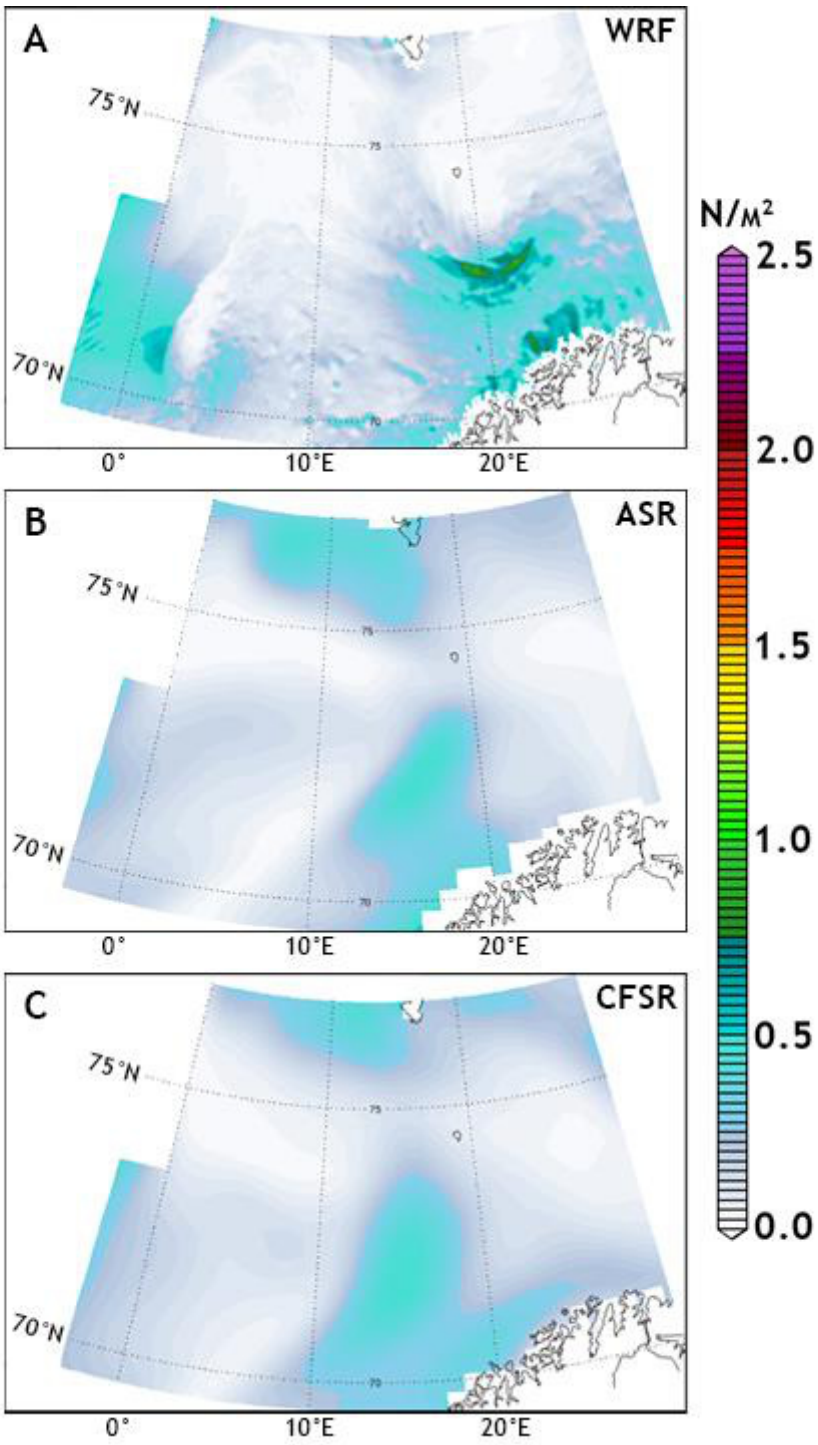

Fig. 14. (a) Shaded momentum flux (N m^{-2}) from a WRF simulation at 0900 UTC 12 December 2006. (b) Shaded momentum flux (N m^{-2}) in ASRv1 data at 0900 UTC 12 December 2006. (c) CFSR Shaded 6-hour average momentum flux (N m^{-2}), averaged from 0600 UTC to 1200 UTC 12 December 2006. The domain shown in these figures is used to gather the information for Fig. 15. Data over land or sea ice is masked out. To remove influence from a cold-air outbreak on analysis, data that are both west of the Greenwich meridian and north of 73.5°N is also masked out (seen in the top-left corner).

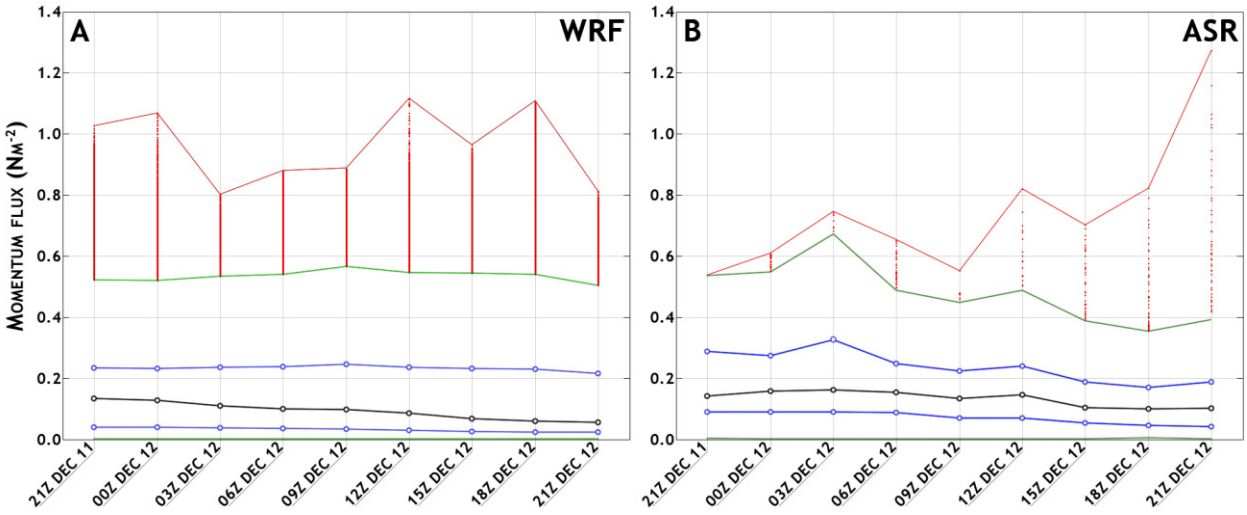

Fig. 15. Distributions of momentum flux (N m^{-2}) from (a) the WRF simulation and (b) ASRv1 for the December 2006 polar mesocyclones shown in Fig. 14. Black lines mark the median of data in the area, and blue lines indicate the 25th and 75th percentiles (τ_{25} and τ_{75} respectively). Green lines demarcate the range of non-extreme values, where values between lines are less than $\tau_{75} + 1.5 \times (\tau_{75} - \tau_{25})$ and greater than $\tau_{25} - 1.5 \times (\tau_{75} - \tau_{25})$. Extreme data are red dots, with maxima and minima marked with red lines.

domain are less than 0.6 N m^{-2} in both sets of data, with the upper quartiles often less than 0.3 N m^{-2}. The discrepancies between the WRF simulation and ASRv1 data are noted, but it is unclear how much impact the differences would have in ocean modeling. Examinations of heat flux (including domain-integrated heat flux) will provide additional insight on potential impacts.

3.3. Heat Flux

Heat flux considers both sensible and latent heat flux, which are expressed as power per unit area (W m^{-2}). Sensible heat flux is the vertical transfer of heat via conduction and convection. Latent heat flux represents the vertical transfer of energy due to latent heat release associated with water phase changes (e.g., condensation). The WRF surface schemes calculate heat fluxes:

$$H = \rho c_p u_* \theta_* \quad (2)$$

$$Q = \rho L_v u_* q_* \quad (3)$$

Equations 2 and 3 represent sensible heat flux and latent heat flux, respectively, where ρ is the air density, c_p is the specific heat of air at constant pressure, L_v is the latent heat of water vaporization, u_* is the friction velocity, q_* is a moisture term analogous to friction velocity, and θ_* is a temperature term analogous to friction velocity.

3.3.1. December 2002 Polar Low

Before the December 2002 polar low developed a hurricane-like form to the west of Novaya Zemlya, a baroclinic zone was situated along the edge of the sea ice, with low 950 – 500 hPa thicknesses oriented over the sea ice and higher thicknesses over the open waters of the Barents Sea (not shown). As the low approached the baroclinic area and induced southward winds, cold-air advection occurred as the air originating over the sea ice was carried over the open water. A cold air outbreak resulted in the wake of the low as it developed into the spiraliform polar low observed herein. Differences in sea surface temperature and 2-meter temperature increased greatly, sometimes in excess of 20°C along the sea ice edge. Around the polar low's center and eyewall, the temperature differences in the simulation and ASRv1 were usually less than 10°C and as low as 4°C (not shown).

The air-sea temperature differences in conjunction with the strong near-surface wind speeds around the storm should be reflected in sensible heat fluxes. The air moving southward off from the sea ice also should contain less moisture than the maritime air over the water, which will impact latent heat fluxes. Sensible heat fluxes at 0600 UTC 19 December 2002 (Fig. 16a – c) appear mostly similar across the WRF simulation and ASRv1 data. The WRF simulation suggests an extension of strong sensible heat fluxes exceeding 700 W m^{-2} just south of the polar low's eye. At the western edge of the domain, ASRv1 produces a larger area of very strong sensible heat

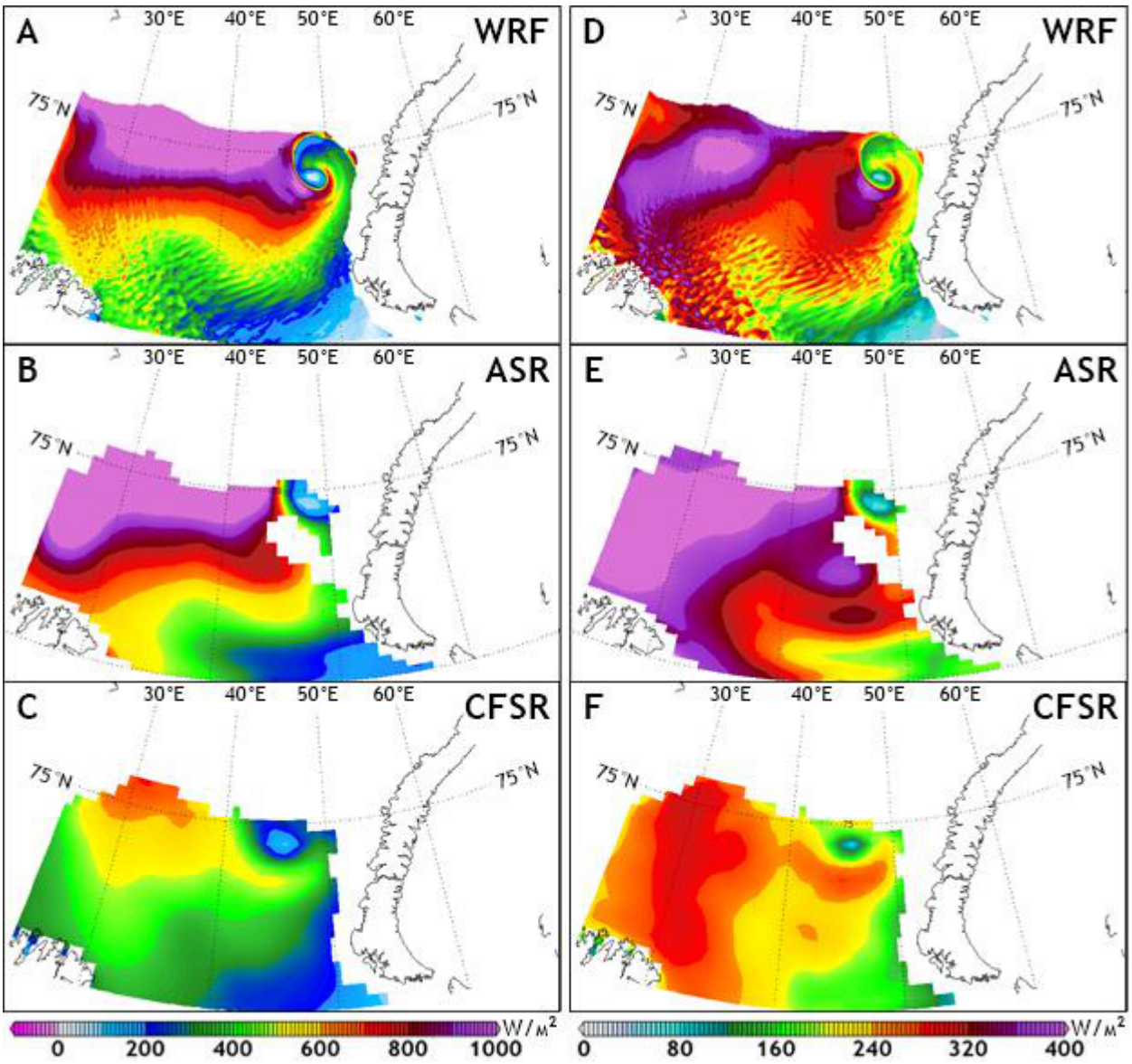

Fig. 16. (a-c) Shaded sensible heat flux (W m^{-2}) from (a) the WRF simulation at 0600 UTC 19 December 2002, (b) ASRv1 data at 0600 UTC 19 December 2002, and (c) CFSR data averaged over 6 hours from 0600 UTC to 1200 UTC 19 December 2002. (d-f) Shaded latent heat flux (W m^{-2}) at the same times as in (a-c) from (d) the WRF simulation, (e) ASRv1 data, and (f) CFSR averaged data. Data are masked out over land and sea ice. The distributions of the data in the domain are shown in Fig. 17.

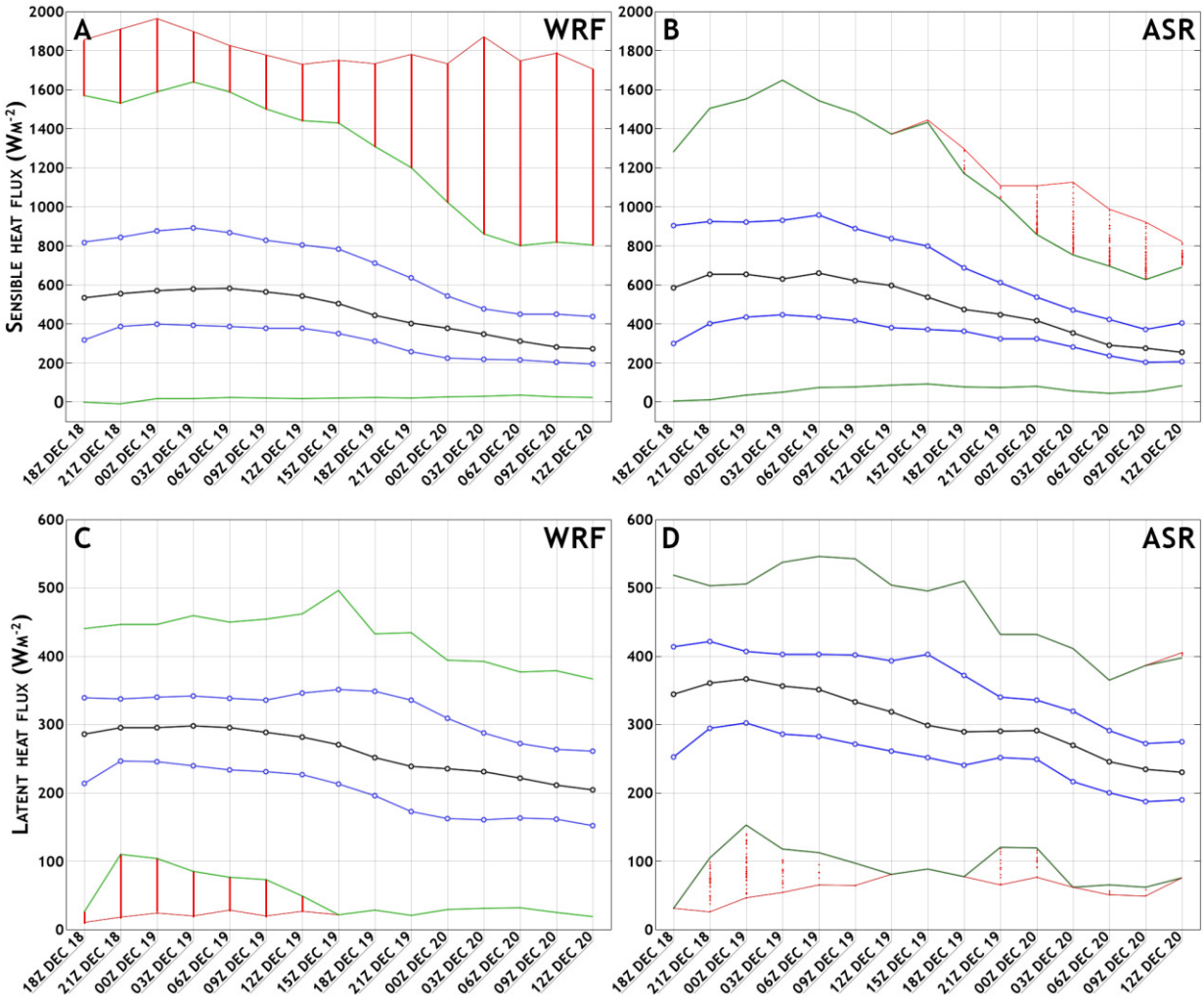

Fig. 17. Distributions of sensible heat flux (top, W m^{-2}) and latent heat flux (bottom, W m^{-2}) from (left; a, c) the WRF simulation and (right; b, d) ASRv1 during the lifetime of the December 2002 polar low. Black lines mark the median of data in the area, and blue lines indicate the 25th and 75th percentiles (H_{25} and H_{75} respectively). Green lines demarcate the range of non-extreme values, where values between lines are less than $H_{75} + 1.5 \times (H_{75} - H_{25})$ and greater than $H_{25} - 1.5 \times (H_{75} - H_{25})$. Extreme data are red dots, with maxima and minima marked with red lines.

fluxes in excess of 1000 W m^{-2}. The gradient of sensible heat flux along the storm's western eyewall is much sharper in the WRF simulation than in ASRv1, which appears to be a result of differing resolutions. The 6-hourly average of sensible heat flux from the CFSR product is substantially weaker along the sea ice edge in comparison to the simulation and ASRv1, with maximum heat fluxes around 700 W m^{-2}.

Distributions of sensible heat flux (Fig. 17) include simulated fluxes of ~1800 W m^{-2}. Sensible heat fluxes exceeding 1400 W m^{-2} are confined to the edge of the sea ice west of the cyclone, where large air-sea temperature differences are located (~20°C difference between sea surface temperature and 2-meter temperature; not shown). Because the sea surface temperatures and sea-ice locations remain constant throughout the simulation, the air-sea temperature differences (and thus, the sensible heat fluxes) are likely affected. A prolonged period of heat flux out from the water and into the atmosphere should decrease the surface temperature over time.

Latent heat fluxes in ASRv1 tend to be greater than those from the simulation (Figs. 16 and 17). For the range of times in Fig. 17, the interquartile range of ASRv1 latent heat flux is always greater than the simulation; and its maximum values also are often greater than the simulation. This difference in maximum latent heat flux implies a discrepancy in the near-surface moisture profile not exclusively dependent on resolution. Averaged latent heat fluxes from CFSR data are often weaker than the simulation and ASRv1, with some local differences being greater than 200 W m^{-2}. Because the distributions of wind stress in ASRv1 for this storm (Fig. 11) suggest greater momentum fluxes over the entire domain compared to the simulation, the stronger latent heat fluxes are likely—in part—a result of stronger wind shear near the surface. Differences between ASRv1 and the simulation in the amount of moisture in the air near the surface can also contribute to differences in the latent heat flux.

3.3.2. December 2006 Polar Low

Air-sea temperature contrasts associated with the December 2006 polar low were not as impressive as those seen in the December 2002 polar low. Therefore, values of sensible heat flux are much smaller. Around the storm, no values of sensible heat flux exceeding 200 W m^{-2} are

evident (Fig. 18a – c). The polar low remained away from sources of frigid air that could potentially translate over warmer open water, moving north-northeast across the Norwegian Sea in the WRF simulation and reanalyses. At 0900 UTC 12 December 2006, ASRv1 reanalyses and CFSR 6-hour averaged data depict areas of weak negative sensible heat flux near the storm (~10 W m^{-2}), while the WRF simulation produces mostly non-negative sensible heat fluxes, especially to the west and northeast of the storm's center (~50 – 100 W m^{-2}). Spatial distributions of sensible heat flux (Fig. 19, top) show a clear difference between the model and ASRv1: The simulation often produces stronger sensible heat fluxes than ASRv1. Upper and lower limits of the interquartile range for the simulation's sensible heat fluxes are often ~25 W m^{-2} greater than those from ASRv1. Readily noticeable areas of negative sensible heat flux appear in ASRv1, because the air-sea temperature differences are reversed in sign—the near-surface air temperature is warmer than the water beneath it. The apparent difference in the near-surface temperature profile between ASRv1 and the WRF simulation does not seem to be a result of differing resolution.

The WRF simulation includes small bands of enhanced latent heat flux (> 200 W m^{-2}; Fig. 18d – f), which the ASRv1 would likely be too coarse to resolve. ASRv1 latent heat fluxes around the polar low at 0900 UTC 12 December 2006 are less than 200 W m^{-2} throughout the domain, while the simulation and the CFSR 0600 UTC – 1200 UTC 12 December 2006 average both have areas of latent heat flux exceeding 200 W m^{-2}. The spread, as well as most magnitudes, of latent heat flux data is greater in the WRF simulation than ASRv1 (Fig. 19, bottom). The lower limit of the interquartile range from ASRv1 data is always less than the WRF simulation, with differences ranging from near zero to ~40 W m^{-2}. Differences in latent heat flux between the model and ASRv1 are linked to the near-surface wind speeds (and subsequently the wind shear and stress), although the latent heat flux is also influenced by the moisture profile and air density near the surface.

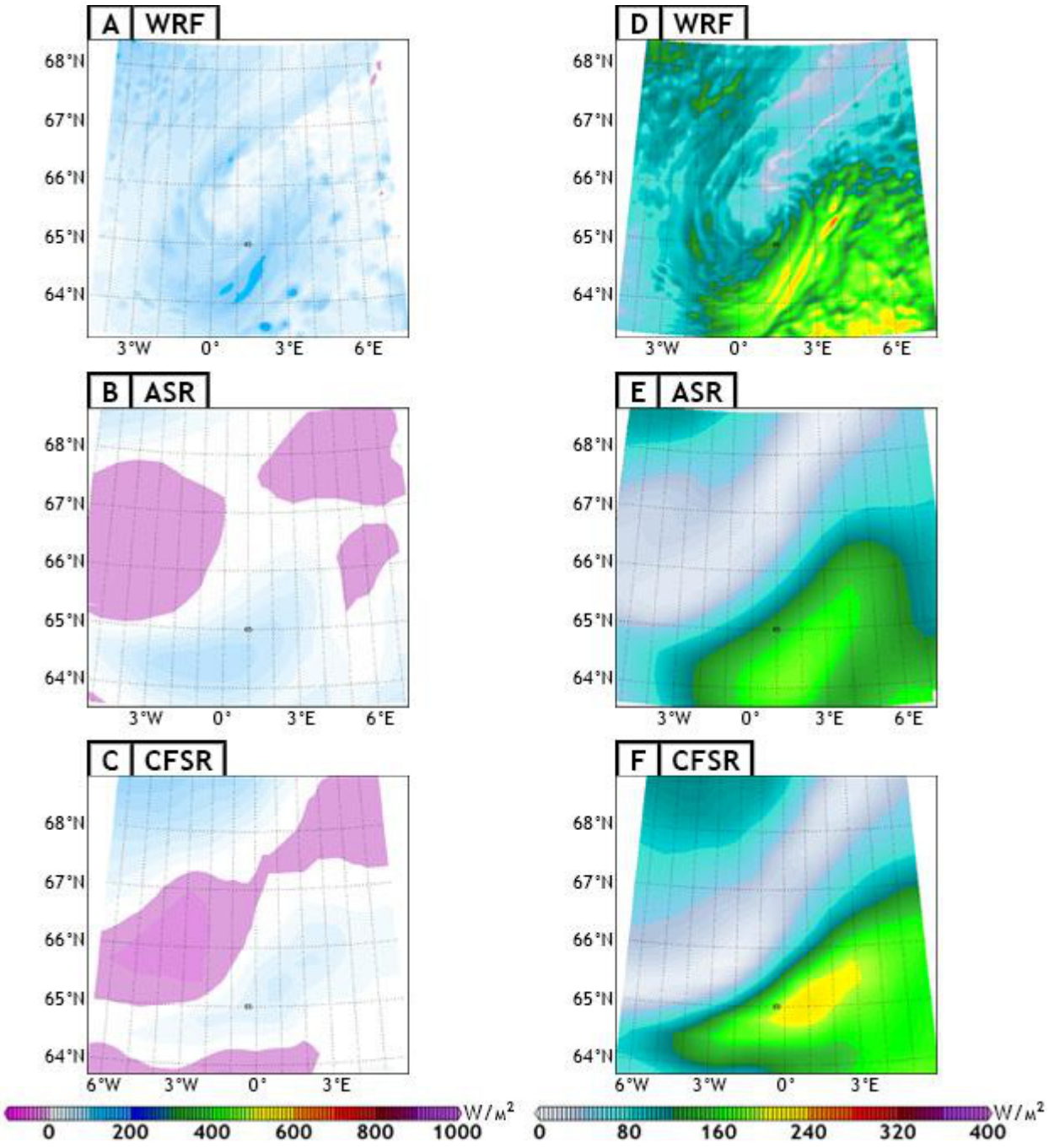

Fig. 18. (a-c) Shaded sensible heat flux (W m^{-2}) from (a) the WRF simulation at 0900 UTC 12 December 2006, (b) ASRv1 data at 0900 UTC 12 December 2006, and (c) CFSR data averaged over 6 hours from 0600 UTC to 1200 UTC 12 December 2006. (d-f) Shaded latent heat flux (W m^{-2}) at the same times as in (a-c) from (d) the WRF simulation, (e) ASRv1 data, and (f) CFSR averaged data.

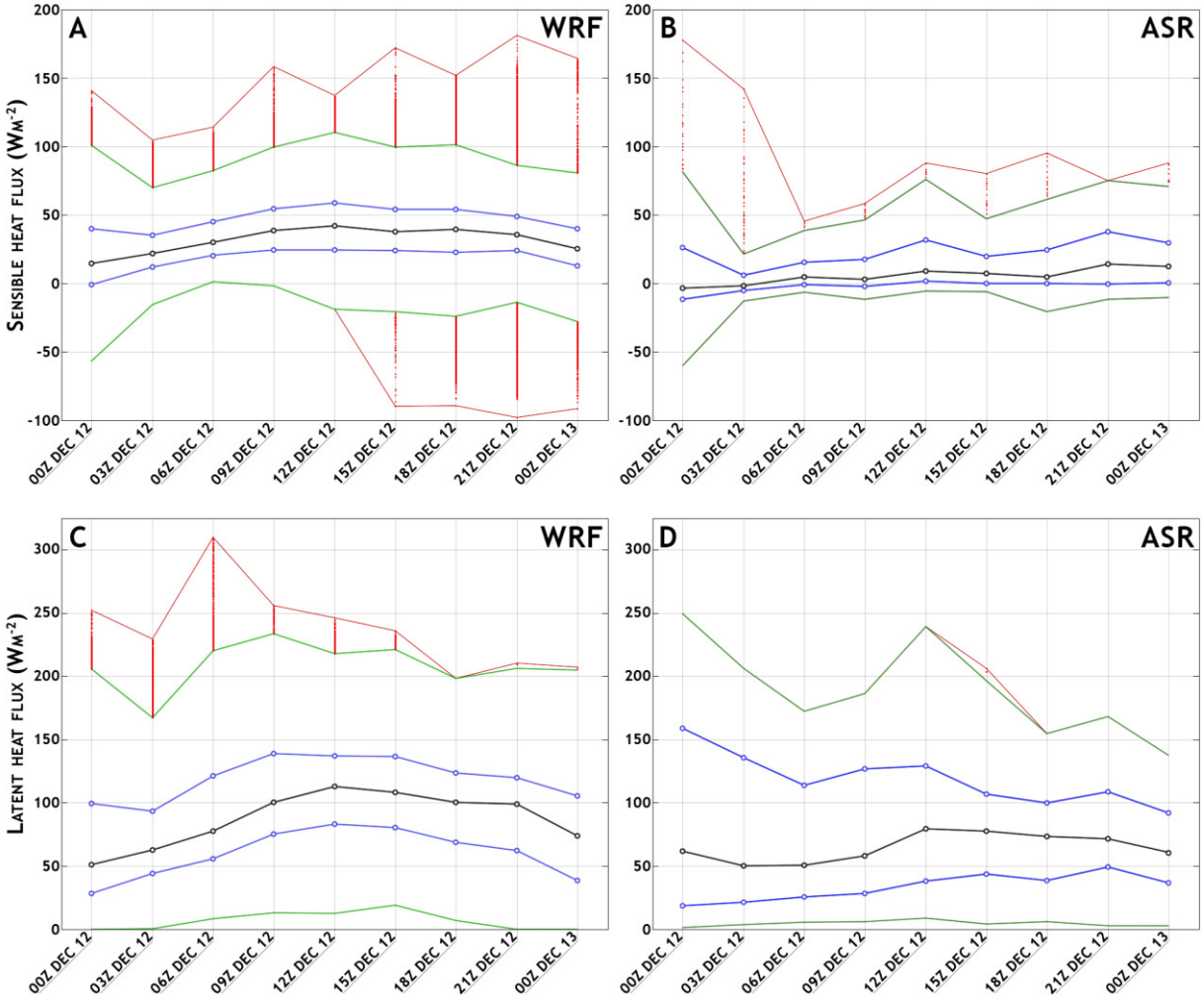

Fig. 19. Distributions of sensible heat flux (top, W m^{-2}) and latent heat flux (bottom, W m^{-2}) from (left; a, c) the WRF simulation and (right; b, d) ASRv1 during the lifetime of the December 2006 polar low. Black lines mark the median of data in the area, and blue lines indicate the 25th and 75th percentiles (H_{25} and H_{75} respectively). Green lines demarcate the range of non-extreme values, where values between lines are less than $H_{75} + 1.5 \times (H_{75} - H_{25})$ and greater than $H_{25} - 1.5 \times (H_{75} - H_{25})$. Extreme data are red dots, with maxima and minima marked with red lines.

The comparisons of the sensible and latent heat fluxes reveal that the WRF simulation produces persistently stronger surface turbulent fluxes associated with this storm than ASRv1. The sensible heat flux comparison implies a difference in the near-surface temperature profile. The warmer air temperatures produced in ASRv1 not only result in negative sensible heat flux, but also lead to lesser values of air density (which is a variable in all surface turbulent flux calculations).

The differences excluding the small-scale amplifications in the WRF simulation (i.e., resolution-based) may be attributed to the near-surface winds and temperatures.

3.3.3. December 2006 Sub-350 km Polar Mesocyclones

The polar mesocyclones south of the Svalbard archipelago are represented differently in the WRF simulation and ASRv1 in analyses of the near-surface wind field, surface and mean sea level pressure, and momentum flux. However, in plots of sensible heat flux and latent heat flux (Fig. 20), the simulation and ASRv1 data appear somewhat similar at 0900 UTC 12 December 2006. A region of negative sensible heat flux (~0 – 25 W m^{-2} in magnitude) is located in the eastern portion of the domain, while an area of increased sensible heat flux extends into the domain from the southwest (~250 W m^{-2} in WRF simulation, ~150 W m^{-2} in ASRv1), likely a result of cold air advection due to westerly flow near Greenland. The CFSR data also present a 6-hour averaged sensible heat flux field (0600 UTC to 1200 UTC) that seems similar to ASRv1 and the WRF simulation at 0900 UTC 12 December 2006, although the area of negative sensible heat flux is larger and covers most of the area north of 73°N. WRF simulated latent heat fluxes at 0900 UTC 12 December increase to 160 – 200 W m^{-2} in the southwest corner of the domain, while ASRv1 data in the same region do not produce latent heat fluxes in excess of 120 W m^{-2}. Throughout, small-scale features that ASRv1 would not be able to resolve appear in the simulation, but the features often have weak amplitudes. Otherwise, the WRF simulation, ASRv1, and the 6-hour averaged latent heat flux from CFSR data do not seem remarkably different. The total air-sea energy transfer associated with the polar mesocyclones may illustrate the cumulative impact of these differences.

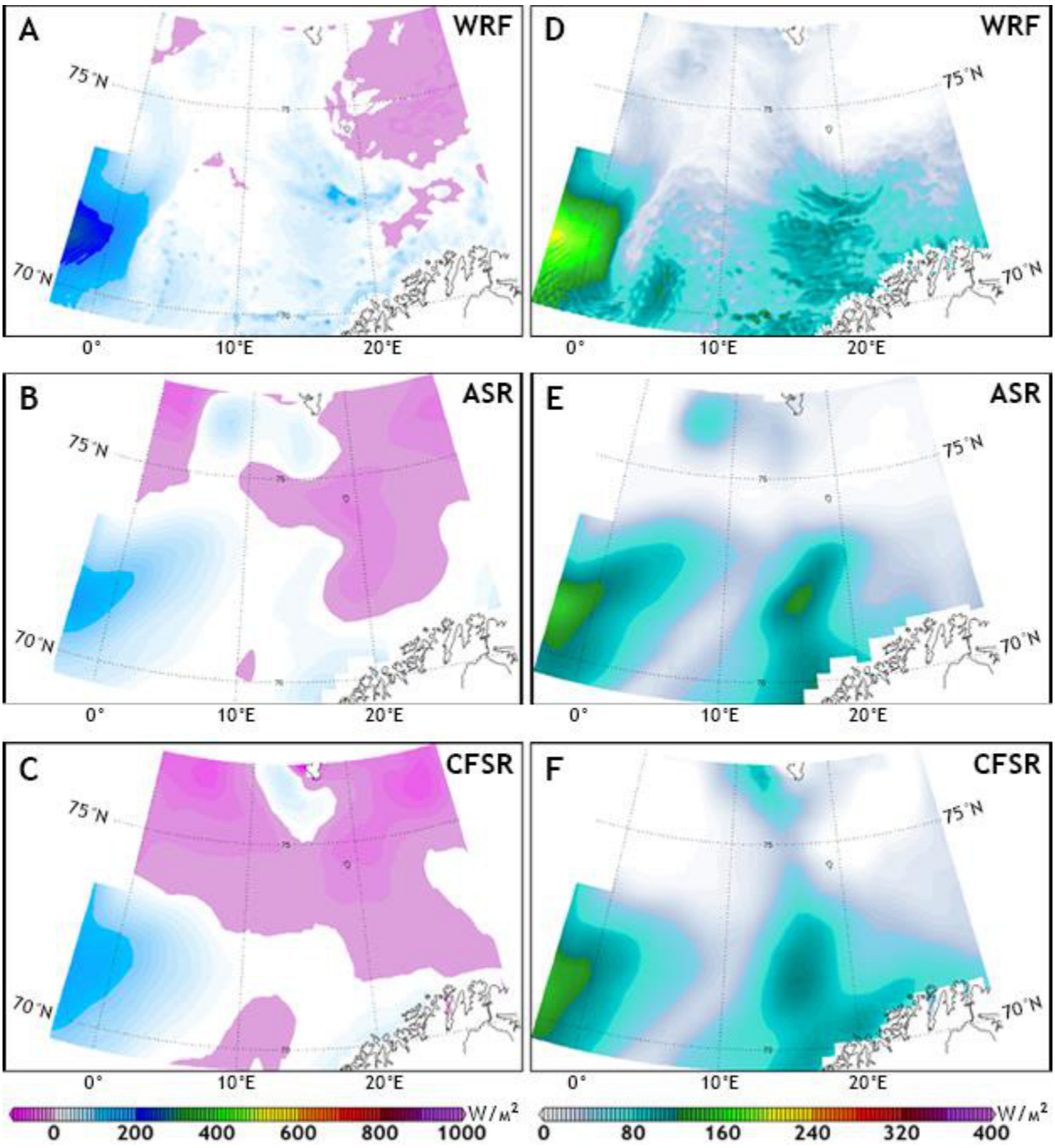

Fig. 20. (a-c) Shaded sensible heat flux (W m^{-2}) from (a) the WRF simulation at 0900 UTC 12 December 2006, (b) ASRv1 data at 0900 UTC 12 December 2006, and (c) CFSR data averaged over 6 hours from 0600 UTC to 1200 UTC 12 December 2006. (d-f) Shaded latent heat flux (W m^{-2}) at the same times as in (a-c) from (d) the WRF simulation, (e) ASRv1 data, and (f) CFSR averaged data. Data are masked out over land. The distributions of the data in the domain are shown in Fig. 21.

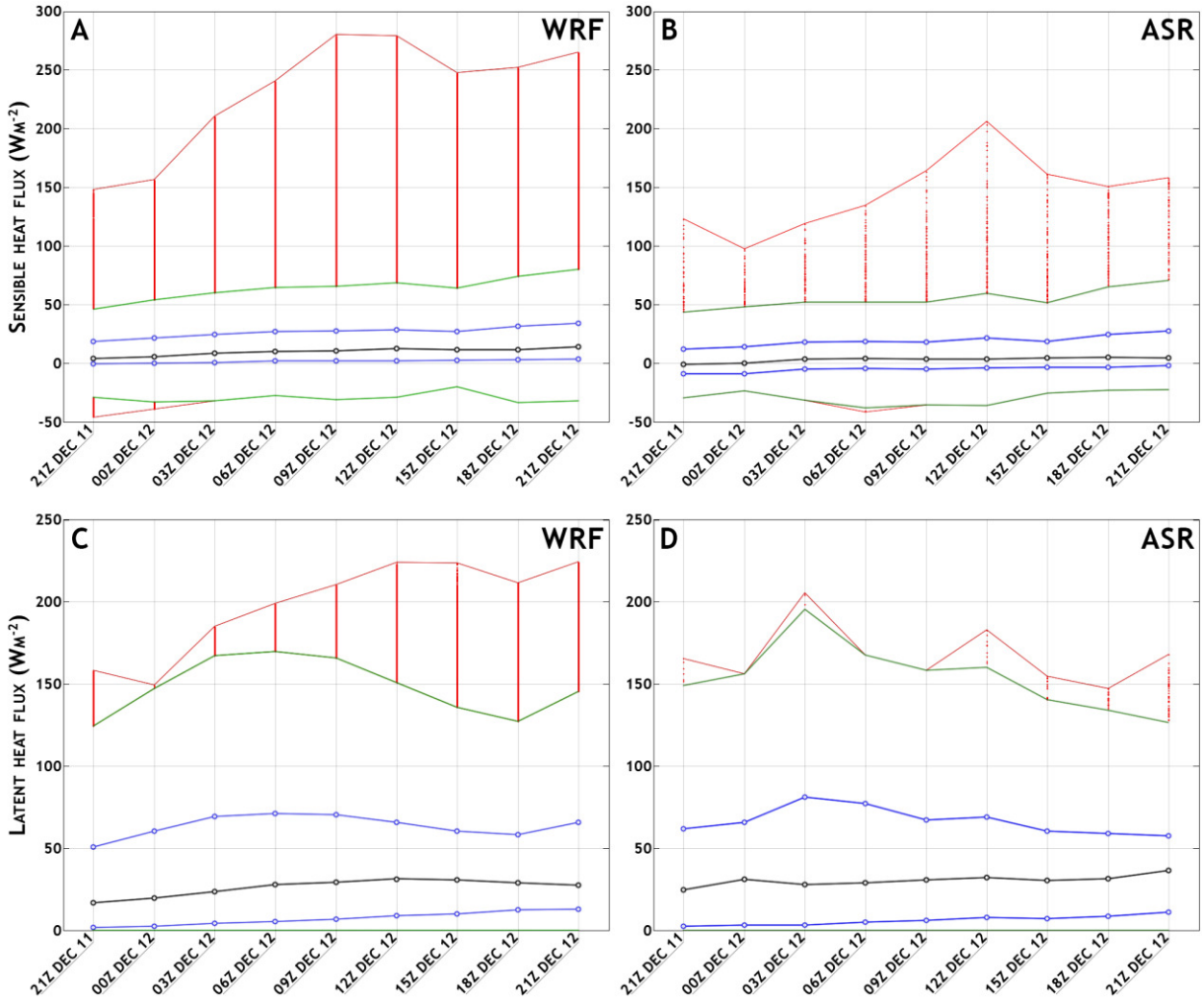

Fig. 21. Distributions of sensible heat flux (top, W m^{-2}) and latent heat flux (bottom, W m^{-2}) from (left; a, c) the WRF simulation and (right; b, d) ASRv1 for the December 2006 polar mesocyclones shown in Fig. 20. Black lines mark the median of data in the area, and blue lines indicate the 25th and 75th percentiles (H_{25} and H_{75} respectively). Green lines demarcate the range of non-extreme values, where values between lines are less than $H_{75} + 1.5 \times (H_{75} - H_{25})$ and greater than $H_{25} - 1.5 \times (H_{75} - H_{25})$. Extreme data are red dots, with maxima and minima marked with red lines.

Considering the domain from 2100 UTC 11 to 2100 UTC 12 December 2006 (Fig. 21), the spreads of data excluding extreme values are very similar. The 25th and 75th percentile lines for sensible heat flux are consistently ~10 W m^{-2} apart between the WRF simulation and ASRv1, with the simulation having the greater sensible heat flux values. Latent heat flux distributions are also similar, with the WRF simulation and ASRv1 interquartile range limits often being less than 10

W m^{-2} different from one another. Extreme values of sensible and latent heat flux are usually stronger in the simulation than in ASRv1. The greatest simulated sensible heat fluxes are ~280 W m^{-2}, which is about 100 W m^{-2} greater than the maximum value from ASRv1 at 0900 UTC 12 December 2006. The extreme heat flux values in the simulation are attributable to cold, drier air entering the domain in the southwest corner of the domain (Fig. 20). Fig. 8 shows the WRF simulation's near-surface winds are stronger than ASRv1 in this region, which suggests stronger heat fluxes from the difference in the near-surface wind profile and more pronounced cold-air advection (from stronger north-northwesterly flow).

The domain-integrated sensible and latent heat fluxes associated with this system are provided in Fig. 22 to illustrate the total amounts of energy transferred at the air-sea boundary. Despite differences in WRF simulated and ASRv1 heat fluxes that appear minimal in Figs. 20 and 21, the total heat flux over the domain of the system is noticeably affected. Throughout the system's lifetime, a domain-integrated total heat flux difference of at least 5 TW (terawatts, 10^{12} W) is evident between ASRv1 and the WRF simulation. Conservatively approximating a 5 TW average domain-integrated heat flux difference over the span of 86400 seconds (1 day) results in a 432 PJ (petajoule, 10^{15} J) difference in energy transferred at the air-sea boundary, which is more than 103 megatons of TNT. The differing presentations of the sub-350 km polar mesocyclones between ASRv1 and the WRF simulation (Fig. 8) produced differing surface turbulent fluxes, which at a glance may appear negligible. However, the calculated cumulative impacts of these storms are greatly affected by the accuracy of surface turbulent fluxes.

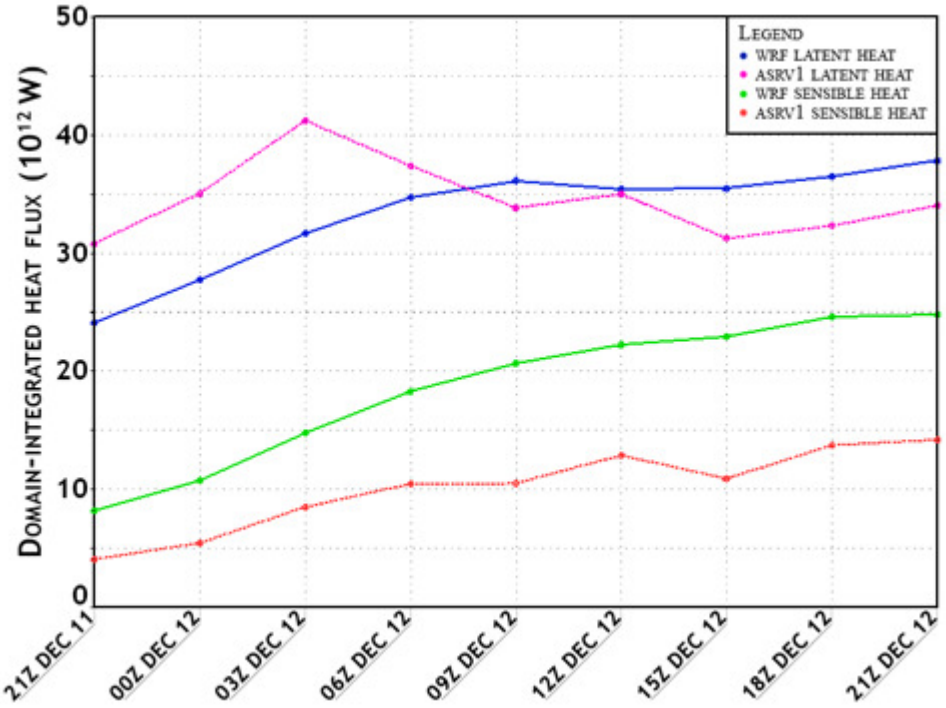

Fig. 22. Domain-integrated sensible and latent heat fluxes (in terawatts, 10^{12} W) for the December 2006 sub-350 km polar mesocyclones. Domain-integrated heat fluxes are obtained by calculating an areal-weighted average of heat flux across the domain (not including masked-out information, as in Figs. 20 and 21), and then multiplying the weighted average by the surface area the flux data occupies. Blue and magenta lines represent WRF simulation and ASRv1 domain-integrated latent heat fluxes, respectively; green and red lines represent WRF simulation and ASRv1 domain-integrated sensible heat fluxes, respectively.

CHAPTER FOUR

CONCLUSIONS AND DISCUSSION

Three systems of polar mesocyclones with varying sizes were modeled and analyzed, specifically for the surface turbulent fluxes they imposed over the open water. Using a reanalysis dataset catered particularly to the arctic—the Arctic System Reanalysis (ASRv1)—with 30 km × 30 km grid spacing and 3-hourly products, comparisons were made against high-resolution (4 km × 4 km) Weather Research and Forecasting (WRF) model simulations. Two questions regarding the representation of polar mesocyclones in ASRv1 were focused on: the ability of ASRv1 to represent progressively smaller polar mesocyclones (i.e., regarding resolution), and the ability of ASRv1 to represent polar mesocyclones on a large enough scale for one to assume its resolution is sufficient (i.e., regarding the physics, dynamics, and information that compose the dataset). Pragmatically, using data with very high spatiotemporal resolution (possibly produced through a model) to prescribe the atmospheric state in an ocean-inclusive climate model is likely not viable due to the sheer amount of resources and time that such a model would require to produce results that would benefit significantly from that data. Thus, it bears emphasizing that the research means only to present the differences between ASRv1 data and a high-resolution simulation to focus on the potential benefits or caveats for using *ASRv1 data* in an ocean model—not very high-resolution model simulation data.

Near-surface winds, momentum fluxes, and heat fluxes were investigated in three polar mesocyclonic systems. The WRF simulation generally produced small-scale, wave-like amplifications of 10 m wind speed, which is included in all surface turbulent flux calculations as part of the friction velocity. These amplifications are likely due to the differing resolution between

ASRv1 and the simulations. However, examinations of sensible and latent heat flux reveal discrepancies regarding near-surface temperature and moisture profiles, which affect calculations of air density (used in all surface turbulent fluxes). These differences are most evident in the December 2006 polar low analysis (Fig. 18), but are also noticeable in latent heat flux analyses of the December 2002 polar low (Fig. 16d – f) and sensible heat flux analyses of the December 2006 sub-350 km polar mesocyclones (Fig. 20a – c). The differences in the near-surface temperature and moisture may be explained physically.

ASRv1 includes updating sea surface temperatures (SSTs) and detailed sea-ice information (including concentration; see Table 1); the WRF simulation uses static sea surface temperature (SST field always equal to SSTs at initialization time) and sea-ice flags (not including concentration, thickness, etc.). These differences have implications on near-surface temperature and moisture profiles, and ASRv1's detailed representations of sea surface temperature and sea-ice fields (compared to the WRF simulation) should be more accurate than the WRF simulation. Therefore, the differences seen in heat fluxes may be a reflection of the WRF simulation's lack of additional SST and sea-ice information. These differences affect air density, thereby affecting momentum fluxes.

ASRv1 appears to represent the examined polar mesocyclones reasonably; the differences between the high-resolution WRF simulation and ASRv1 seemed to be a result of either resolution or the physical make-up of the data (e.g., detailed sea-ice information in ASRv1). The WRF model simulation seems to have stronger small-scale surface turbulent fluxes than the ASRv1 dataset, which may be attributed to ASRv1's resolution. A set of WRF model simulations with 30 km × 30 km grid spacing will be run in the future to investigate differences independent of resolution. However, though several differences are noted herein, the impact of such differences should be

examined in ocean modeling. Further, the cumulative effect of many polar mesocyclones in a region over time has not been addressed, which would require a comprehensive analysis including many more storms over a sufficient time period. From the domain-integrated heat fluxes provided for the December 2006 sub-350 km polar mesocyclones (Fig. 22), it appears that accuracy in representing fluxes is critical in establishing reasonable air-sea interaction over time.

REFERENCES

Bacon, S., 1998: Decadal variability in the outflow from the Nordic seas to the deep Atlantic Ocean. *Nature*, **394**, 871 – 874.

Beljaars, A. C. M., 1994: The parameterization of surface fluxes in large-scale models under free convection. *Quart. J. Roy. Meteor. Soc.*, **121**, 255 – 270.

Bentsen, M., H. Drange, T. Furevik, and T. Zhou, 2004: Simulated variability of the Atlantic meridional overturning circulation. *Climate Dyn.*, **22**, 701 – 720.

Bigg, G. R., S. R. Dye, and M. R. Wadley, 2005: Interannual variability in the 1990s in the northern Atlantic and Nordic Seas. *J. Atmos. Ocean Sci.*, **10**(2), 123 – 143, doi: 10.1080/17417530500282873.

Brodeau, L., B. Barnier, A.-M. Treguier, T. Penduff, and S. Gulev, 2010: An ERA40-based atmospheric forcing for global ocean circulation models. *Ocean Model.*, **31**, 88 – 104.

Bromwich, D. H., K. M. Hines, and L.-S. Bai, 2009: Development and testing of Polar WRF: 2. Arctic Ocean. *J. Geophys. Res*., **114**, D08122, doi:10.1029/2008JD010300.

Bromwich, D. H., Y.-H. Kuo, M. Serreze, J. Walsh, L.-S. Bai, M. Barlage, K. M. Hines, and A. Slater, 2010: Arctic System Reanalysis: Call for community involvement. *Eos Trans. Amer. Geophys. Union*, **91**(2), 13 – 14.

Bromwich, D. H., A. B. Wilson, L. Bai, G. W. K. Moore, and P. Bauer, 2015: A comparison of the regional Arctic System Reanalysis and the global ERA-Interim reanalysis for the arctic. *Quart. J. Roy. Meteor. Soc.*, in press, 45 pp.

Cardona, Y., and A. Bracco, 2012: Enhanced vertical mixing within mesoscale eddies due to high frequency winds in the South China Sea. *Ocean Model.*, **42**, 1 – 15.

Chelton, D. B., and M. H. Freilich, 2005: Scatterometer-based assessment of 10-m wind analyses from the operational ECMWF and NCEP numerical weather prediction models. *Mon. Wea. Rev.*, **133**, 409 – 429.

Chen, D., W. T. Liu, S. E. Zebiak, M. A. Cane, Y. Kushnir, and D. Witter, 1999: Sensitivity of the tropical Pacific Ocean simulation to the temporal and spatial resolution of wind forcing. *J. Geophys. Res.*, **104**, 11261 – 11271.

Chen, F., K. W. Manning, M. A. LeMone, S. B. Trier, J. G. Alfieri, R. Roberts, M. Tewari, D. Niyogi, T. W. Horst, S. P. Oncley, J. B. Basara, and P. D. Blanken, 2007: Description and evaluation of the characteristics of the NCAR high-resolution land data assimilation system. *J. Appl. Meteor. Climatol.*, **46**, 694 – 713, doi: 10.1175/JAM2463.1.

Chou, M.-D., and M. J. Suarez, 1994: An efficient thermal infrared radiation parameterization for use in general circulation models. NASA Tech. Memo. 104606, Vol. 3, 84 pp.

Clark, P. U, N. G. Pisias, T. F. Stocker, and A. J. Weaver, 2002: The role of the thermohaline circulation in abrupt climate change. *Nature*, **415**, 863 – 869, doi:10.1038/415863a.

Claud, C., G. Heinemann, E. Raustein, and L. Mcmurdie, 2004: Polar low *le Cygne*: Satellite observations and numerical simulations. *Quart. J. Roy. Meteor. Soc.*, **130**, 1075 – 1102.

Condron, A., G. R. Bigg, and I. A. Renfrew, 2006: Polar mesoscale cyclones in the northeast Atlantic: Comparing climatologies from ERA-40 and satellite imagery. *Mon. Wea. Rev.*, **134**, 1518 – 1533.

Condron, A., G. R. Bigg, and I. A. Renfrew, 2008: Modeling the impact of polar mesocyclones on ocean circulation. *J. Geophys. Res.,* **113**, C10005, doi:10.1029/2007JC004599.

Dee, D. P., S. M. Uppala, A. J. Simmons, P. Berrisford, P. Poli, S. Kobayashi, U. Andrae, M. A. Balmaseda, G. Balsamo, P. Bauer, P. Bechtold, A. C. M. Beljaars, L. van de Berg, J. Bidlot, N. Bormann, C. Delsol, R. Dragani, M. Fuentes, A. J. Geer, L. Haimberger, S. B. Healy, H. Hersbach, E. V. Hólm, L. Isaksen, P. Kållberg, M. Köhler, M. Matricardi, A. P. McNally, B. M. Monge-Sanz, J.-J. Morcrette, B.-K. Park, C. Peubey, P. de Rosnay, C. Tavolato, J.-N. Thépaut, and F. Vitart, 2011: The ERA-Interim reanalysis: configuration and performance of the data assimilation system. *Quart. J. Roy. Meteor. Soc.*, **137**, 553 – 597.

Dyer, A. J., and B. B. Hicks, 1970: Flux-gradient relationships in the constant flux layer. *Quart. J. Roy. Meteor. Soc.*, **96**, 715 – 721.

Fore, A. G., B. W. Stiles, A. H. Chau, B. A. Williams, R. S. Dunbar, and E. Rodríguez, 2014: Point-wise wind retrieval and ambiguity removal improvements for the QuikSCAT climatological data set. *IEEE Trans. Geosci. Remote Sens.*, **52**, 51 – 59, doi:10.1109/TGRS.2012.2235843.

Føre, I., J. E. Kristjánsson, E. W. Kolstad, T. J. Bracegirdle, Ø. Saetra, and B. Røsting, 2012: A 'hurricane-like' polar low fuelled by sensible heat flux: high-resolution numerical simulations. *Quart. J. Roy. Meteor. Soc.*, **138**, 1308 – 1324, doi:10.1002/qj.1876.

Gentry, M. S., and G. M. Lackmann, 2010: Sensitivity of simulated tropical cyclone structure and intensity to horizontal resolution. *Mon. Wea. Rev.*, **138**, 688 – 704.

Gulev, S. K., B. Barnier, H. Knochel, J.-M. Molines, and M. Cottet, 2003: Water mass transformation in the North Atlantic and its impact on the meridional circulation: Insights from an ocean model forced by NCEP-NCAR reanalysis surface fluxes. *J. Climate*, **16**, 3085 – 3110.

Häkkinen, S., 1999: Variability of the simulated meridional heat transport in the North Atlantic for the period 1951–1993. *J. Geophys. Res.*, **104**, 10991 – 11007.

Harold, J. M., G. R. Bigg, and J. Turner, 1999: Mesocyclone activity over the northeast Atlantic, part 1: Vortex distribution and variability. *Int. J. Climatol.*, **19**, 1187 – 1204.

Hines, K. M., and Bromwich D. H., 2008: Development and testing of Polar WRF. Part I: Greenland ice sheet meteorology. *Mon. Wea. Rev.*, **136**, 1971 – 1989, doi:10.1175/2007MWR2112.1.

Hines, K. M., D. H. Bromwich, L.-S. Bai, M. Barlage, and A. G. Slater, 2011: Development and testing of Polar WRF: Part III. Arctic Land. *J. Climate*, **24**, 26 – 48, doi:10.1175/2010JCLI3460.1.

Hong, S.-Y., Y. Noh, and J. Dudhia, 2006: A new vertical diffusion package with explicit treatment of entrainment processes. *Mon. Wea. Rev.*, **134**, 2318–2341.

Iacono, M. J., J. S. Delamere, E. J. Mlawer, M. W. Shephard, S. A. Clough, and W. D. Collins, 2008: Radiative forcing by long-lived greenhouse gases: Calculations with the AER radiative transfer models. *J. Geophys. Res.*, **113**, D13103.

Kain, J. S., and J. M. Fritsch, 1990: A one-dimensional entraining-detraining plume model and its application in convective parameterization. *J. Atmos. Sci.*, **47**, 2784 – 2802.

Kain, J. S., and J. M. Fritsch, 1993: Convective parameterization for mesoscale models: The Kain-Fritsch scheme. *The Representation of Cumulus Convection in Numerical Models, Meteor. Monogr.*, No. 46. Amer. Meteor. Soc., 165 – 170.

Kain, J. S., 2004: The Kain-Fritsch convective parameterization: An update. *J. Appl. Meteor.*, **43**, 170 – 181.

Kelly, K. A., S. Dickenson, and Z. Yu, 1999: NSCAT tropical wind stress maps: Implications for improving ocean modeling. *J. Geophys. Res.*, **104**, 11291 – 11310.

Latif, M., C. Böning, J. Willebrand, A. Biastoch, J. Dengg, N. Keenlyside, U. Schweckendiek, and G. Madek, 2006: Is the thermohaline circulation changing? *J. Climate*, **19**, 4631 – 4637.

Liu, W. T., 2002: Progress in scatterometer application. *J. Oceanogr.*, **58**, 121 – 136.

Marshall, J., and F. Schott, 1999: Open ocean convection: Observations, theory and models. *Rev. Geophys.*, **37**(1), 1–64.

McManus, J. F., R. Francois, J.-M. Gherardi, L. D. Keigwin, and S. Brown-Leger, 2004: Collapse and rapid resumption of Atlantic meridional circulation linked to deglacial climate changes. *Nature*, **428**, 834 – 837, doi:10.1038/nature02494.

Moore, G. W. K., 2012: A new look at Greenland flow distortion and its impact on barrier flow, tip jets and coastal oceanography. *Geophys. Res. Lett.*, **39**, L22806, doi:10.1029/2012GL054017.

Nakanishi, M., 2001: Improvement of the Mellor-Yamada turbulence closure model based on large-eddy simulation data. *Boundary Layer Meteorol.*, **99**, 349 – 378.

Nakanishi, M., and H. Niino, 2004: An improved Mellor-Yamada level-3 model with condensation physics: Its design and verification. *Boundary Layer Meteorol.*, **112**, 1 – 31.

Nakanishi, M., and H. Niino, 2006: An improved Mellor-Yamada level-3 model. Its numerical stability and application to a regional prediction of advection fog. *Boundary Layer Meteorol.*, **119**, 397 – 407.

Onogi, K., J. Tsutsui, H. Koide, M. Sakamoto, S. Kobayashi, H. Hatsushika, T. Matsumoto, N. Yamazaki, H. Kamahori, K. Takahashi, S. Kadokura, K. Wada, K. Kato, R. Oyama, T. Ose, N. Mannoji, and R. Taira, 2007: The JRA-25 reanalysis. *J. Meteor. Soc. Japan*, **85**, 369 – 432.

Paulson, C. A., 1970: The mathematical representation of wind speed and temperature profiles in the unstable atmospheric surface layer. *J. Appl. Meteor.*, **9**, 857 – 861.

Pickart, R. S., M. A. Spall, M. H. Ribergaard, G. W. K. Moore, and R. F. Milliff, 2003: Deep convection in the Irminger Sea forced by the Greenland tip jet. *Nature*, **424**, 152 – 156.

Pickart, R. S., and M. A. Spall, 2007: Impact of Labrador Sea convection on the North Atlantic meridional overturning circulation. *J. Phys. Oceanogr.*, **37**, 2207 – 2227.

Rahmstorf, S., 1995: Bifurcations of the Atlantic thermohaline circulation in response to changes in the hydrological cycle. *Nature*, **378**, 145 – 149, doi:10.1038/378145a0.

Rahmstorf, S., 1996: On the freshwater forcing and transport of the Atlantic thermohaline circulation. *Climate Dyn.*, **12**, 799 – 811.

Rasmussen, E. A., and J. Turner, 2003: *Polar Lows: Mesoscale Weather Systems in the Polar Regions*. 612 pp., Cambridge Univ. Press, New York.

Renfrew, I. A., G. W. K. Moore, J. E. Kristjánsson, H. Ólafsson, S. L. Gray, G. N. Petersen, K. Bovis, P. R. A. Brown, I. Føre, T. Haine, C. Hay, E. A. Irvine, A. Lawrence, T. Ohigashi, S. Outten, R. S. Pickart, M. Shapiro, D. Sproson, R. Swinbank, A. Woolley, and S. Zhang, 2008: The Greenland flow distortion experiment. *Bull. Am. Meteorol. Soc.*, **89**, 1307 – 1324, doi:10.1175/2008BAMS2508.1.

Saha, S. and Coauthors, 2006: The NCEP Climate Forecast System. *J. Climate,* **19**, 3483 – 3517.

Simmons, A. J., and J. K. Gibson, 2000: The ERA-40 project plan. [Available online at http://old.ecmwf.int/publications/library/ecpublications/_pdf/era40/ERA40_PRS_1.pdf .]

Skamarock, W. C., Klemp, J. B., Dudhia, J., Gill, D. O., Barker, D. M., Duda, M., Huang, X.-Y., Wang, W., and Powers, J. G., 2008: A Description of the Advanced Research WRF Version 3, NCAR Technical Note.

Tao, W.-K., and J. Simpson, 1993: The Goddard Cumulus Ensemble model. Part I. Model description. *Terr. Atmos. Ocean. Sci.*, **4**, 19 – 54.

Tao, W.-K., J. Simpson, D. Baker, M.-D. Chou, B. Ferrier, D. Johnson, A. Khain, S. Lang, B. Lynn, C.-L. Shie, D. Starr, C.-H. Sui, Y. Wang, and P. Wetzel, 2003: Microphysics, radiation and surface processes in the Goddard Cumulus Ensemble (GCE) model. *Meteorol. Atmos. Phys.*, **82**, 97 – 137.

Tewari, M., F. Chen, W. Wang, J. Dudhia, M. A. LeMone, K. Mitchell, M. Ek, G. Gayno, J. Wegiel, and R. H. Cuenca, 2004: Implementation and verification of the unified NOAH land surface model in the WRF model. *20th conference on weather analysis and forecasting/16th conference on numerical weather prediction*, Seattle, WA, American Meteorological Society.

Thompson, G., P. R. Field, R. M. Rasmussen, and W. D. Hall, 2008: Explicit forecasts of winter precipitation using an improved bulk microphysics scheme. Part II: Implementation of a new snow parameterization. *Mon. Wea. Rev.*, **132**, 519–542.

Webb, E. K., 1970: Profile relationships: The log-linear range, and extension to strong stability. *Quart. J. Roy. Meteor. Soc.*, **96**, 67 – 90.

Zhang, D.-L., and R. A. Anthes, 1982: A high-resolution model of the planetary boundary layer—sensitivity tests and comparisons with SESAME-79 data. *J. Appl. Meteor.*, **21**, 1594 – 1609.

BIOGRAPHICAL SKETCH

Kyle Ahern is a graduate student at the Florida State University working for Dr. Mark Bourassa. He has interests in several meteorological topics, including polar meteorology and climatology, tropical meteorology, and mesoscale severe weather. Kyle became a National Oceanic and Atmospheric Administration's Ernest F. Hollings scholar in his sophomore year. He completed a student project at the Anchorage, Alaska Weather Forecasting Office over nine weeks, where he studied synoptic and mesoscale patterns causing ice storms and freezing rain events. In 2013, Kyle graduated with honors and a perfect GPA at the Florida State University. His undergraduate research on convective transport in Southeast Asia with Dr. Henry Fuelberg earned the American Meteorological Society's James B. Macelwane award in 2013. He is a member of Phi Beta Kappa and received the Marion Jewell Hay award for his undergraduate research, which is given to the top graduating senior completing an honors thesis at the Florida State University.